# SeaWinds ALGORITHM THEORETICAL BASIS DOCUMENT

**M.H. Freilich, P.I.**

## 1. Introduction

Knowledge of wind velocity over the ocean is of critical importance for understanding and predicting many oceanographic, meteorological, and climate phenomena. Wind stress is the single largest source of momentum to the upper ocean, and winds drive oceanic motions on scales ranging from surface waves to basin-wide current systems. Winds over the oceans regulate the crucial coupling between the air and the sea that maintains global and regional climate, by modulating air-sea fluxes of heat, moisture, and chemical substances. Measurements of surface wind velocity can be assimilated into regional and global numerical weather prediction systems, thereby extending and improving our ability to predict future weather patterns on many scales.

All presently available ocean wind velocity data sets are deficient in coverage and accuracy. Ship reports are geographically and phenomenologically biased and are inaccurate owing to untrained observers, poor instrumentation, badly placed anemometers, inadequate correction for ship velocity, and data transcription and transmission errors (Pierson, 1990). Measurements from moored meteorological buoys are highly accurate (Gilhousen, 1987), but they are few in number and tend to be concentrated in near-coastal regions in the northern hemisphere. Only satellite-borne instruments can acquire wind data with global coverage, high spatial resolution, and frequent sampling.

In particular, satellite-borne radar scatterometers are the only remote sensing systems presently capable of providing accurate, frequent, high-resolution measurements of ocean near-surface wind speed and direction in both clear-sky and cloudy conditions. However, scatterometer measurements are highly indirect, and significant processing is required to estimate near-surface wind velocity from the backscattered power measured directly by the scatterometer. A Ku-band scatterometer "SeaWinds," will fly during the EOS era. It is the purpose of this document to describe the theoretical bases for the major scientific algorithms that will be used in processing the SeaWinds (SWS) data.

This document is organized as follows. General principles of scatterometry, including the model func-

tion function relating backscatter cross-section to wind and radar parameters, are discussed in section 2.1. Brief descriptions of previous (section 2.2) and planned (section 2.3) spaceborne scatterometer instruments follow. The experimental objectives and key mission requirements for the SWS experiment, including a summary of the SWS standard products, are presented in section 2.4. A brief description of the SWS flight instrument design is given in section 2.5. Following introductory outlines of the SWS algorithm development philosophy and the relationship between SWS and NSCAT algorithms (section 3.1), major science algorithms for radar cross-section calculation, radar cross-section correction for atmospheric attenuation using colocated microwave radiometer data, wind retrieval, and ambiguity removal are presented in sections 3.2–3.5, respectively. These subsections include both the theoretical bases for the mathematical calculations and algorithmic/numerical approaches where known.

## 2. Overview and Background Information

### *2.1 Principles of scatterometry*

Remote measurement of surface wind velocity using active microwave scatterometers is a relatively mature technique, although only two complete scatterometer instruments have actually flown in space. General principles of scatterometry, as well as aspects of airborne and spaceborne hardware design and ground data processing are discussed in texts by Ulaby et al. (1981, 1982, 1986), Stewart (1985), and Elachi (1988). An open-literature summary, with specific focus on the NSCAT scatterometer, can be found in Naderi et al. (1991). Therefore, only a brief outline is given here.

Scatterometers are microwave radar instruments designed specifically to acquire accurate, multiple measurements of the radar cross-section of the ocean surface. Estimates of near-surface wind velocity and related quantities such as the horizontal component of wind stress can be obtained by combining spatially and temporally colocated backscatter measurements acquired from different viewing geometries.

#### *2.1.1 Backscatter cross-section ($\sigma_0$) measurement*

Spaceborne scatterometers transmit microwave pulses to the ocean surface and measure the backscattered power received at the instrument. Since the atmospheric motions themselves do not substantially affect the radiation emitted and received by the radar, scatterometer measurements of wind velocity are highly indirect. Momentum transferred from the air to the sea by the wind causes the surface of the ocean to become rough. Changes in wind velocity cause changes in surface roughness, which in turn modify the radar cross-section of the ocean and hence the magnitude of the backscattered power. Scatterometers measure this backscattered power, allowing estimation of the normalized radar cross-section ($\sigma_0$) of the sea surface.

For each illuminated location on the earth, the total received power $P_r$ is the sum of the backscattered power $P_b$ and a contribution $P_n$ resulting from instrument noise and the natural emissivity (at that frequency) from the earth-atmosphere system. In order to determine $P_b$ accurately, the noise power $P_n$ must be estimated and subtracted from the total received power $P_r$; the radar equation (Ulaby et al., 1981, 1982, 1986; see section 3.2) can then be used to calculate $\sigma_0$. This subtraction, driven by the requirement for accurate absolute measurements of $\sigma_0$, is a unique feature of scatterometers, and sets them apart from other active

microwave remote sensing instruments such as altimeters and synthetic aperture radars.

### *2.1.2 Model function*

In order to extract wind velocity information from $\sigma_0$ measurements, the relationship between radar cross-section and near-surface winds must be known. Although not an algorithm per se, the model function relating $\sigma_0$ to environmental conditions and radar parameters (including imaging geometry) plays a crucial role in the design of scatterometer instruments and the ground processing of the data acquired. The functional and numerical treatment of the model function likewise places strong constraints on, and vitally effects the flexibility of, the wind retrieval algorithms.

In its general form, the model function can be written:

$$\sigma_0 = M(w, \chi, \ldots; \theta, \mathrm{p}, f) \tag{1}$$

where $\sigma_0$ is the normalized radar cross-section of the sea surface, $w$ and $\chi$ are respectively the "wind speed" and relative wind direction (the angle, measured in the horizontal plane, between the wind and the radar illumination direction), and "..." represent dependences on subsidiary, non-wind geophysical variables such as atmospheric boundary layer stratification, long wave conditions, sea-surface temperature, etc. Radar and geometric parameters $\theta$, p, and $f$ denote incidence angle, polarization (typically vertical or horizontal), and radar frequency, respectively. Although questions remain regarding the specific wind-like property to which $\sigma_0$ is most closely related (wind velocity at a specific height, neutral stability wind velocity at a height, friction velocity, or stress itself), this document will use the terms "wind velocity" or "vector wind." Likewise, the terms "speed" and "direction" will be used to denote the magnitude and direction of the quantity.

A scatterometer's ability to measure vector winds derives from the fact that $\sigma_0$ is a sensitive function both of wind speed $w$ and relative direction $\chi$. The wind speed dependence of the SASS-2 model (Wentz et al., 1984) at the 48° (h-pol) and 55° (v-pol) incidence angles measured by SWS (see section 2.4) is shown in figure 1, and the relative direction dependences are shown in figure 2 for a variety of wind speeds. It is seen that $\sigma_0$ (in dB) increases approximately linearly with $\log(w)$ at fixed azimuth. Likewise, the relationship between $\sigma_0$ and $\chi$ is nearly $\cos(2\chi)$, with $\sigma_0$ having maxima at upwind ($\chi = 0°$) and downwind ($\chi = 180°$) and minima near crosswind ($\chi = 90°$ and $270°$ ). This upwind-crosswind modulation of $\sigma_0$ forms the basis

for the measurement of wind direction by scatterometers. At Ku-band frequencies, the upwind-crosswind ratio increases with increasing incidence angle, is typically larger for h-pol than for v-pol, and is largest at low wind speeds.

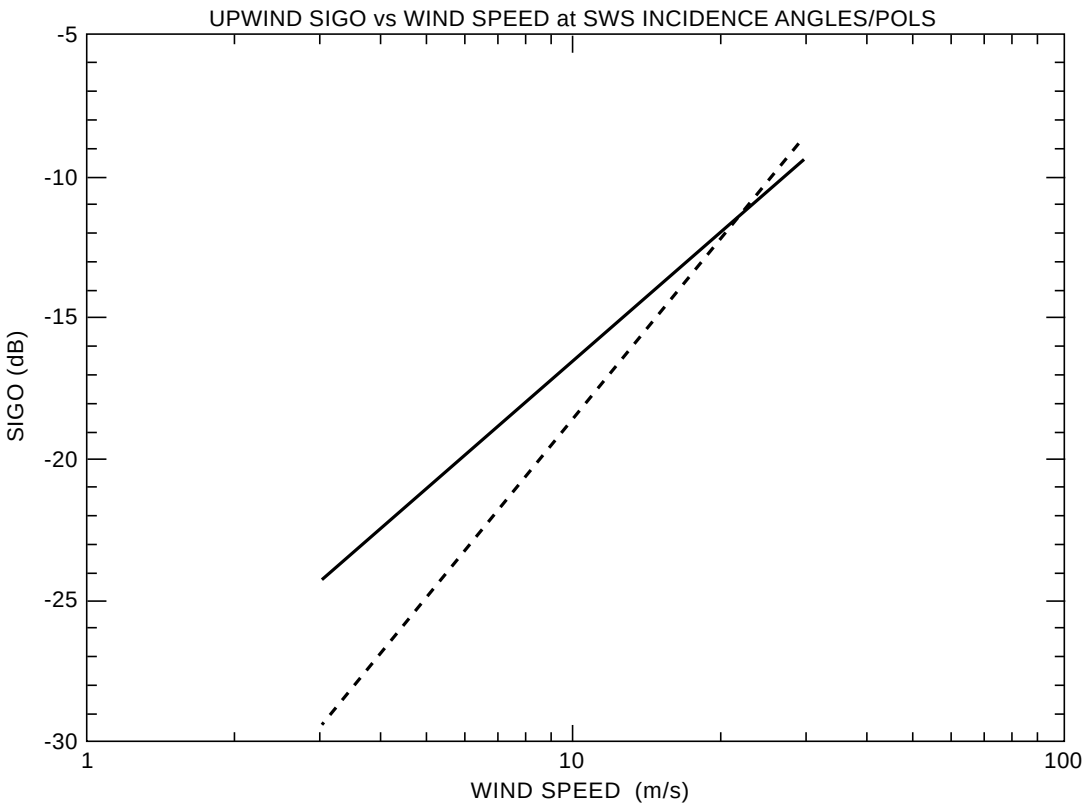


Figure 1. Variation of $\sigma_0$ (dB) with wind speed (m/s) as predicted by the SASS-2 model function; upwind direction ($\chi = 0$) at the SeaWinds incidence angles of 47° (h-pol) and 55° (v-pol).

There is also an important, although small, difference in $\sigma_0$ between upwind and downwind directions, with upwind cross-sections generally larger than downwind. In the absence of this asymmetry, scatterometer wind vector measurements would always result in a 180° ambiguity in direction (it would be impossible to determine whether the wind was blowing "from" or "to" a given direction based on even perfect scatterometer measurements). The upwind-downwind asymmetry makes it possible in principle to determine a unique wind vector, although errors in the $\sigma_0$ measurements generally make it extremely difficult to choose the correct ambiguity based on $\sigma_0$ measurements from a single wind vector cell (see section 3.5). As with the

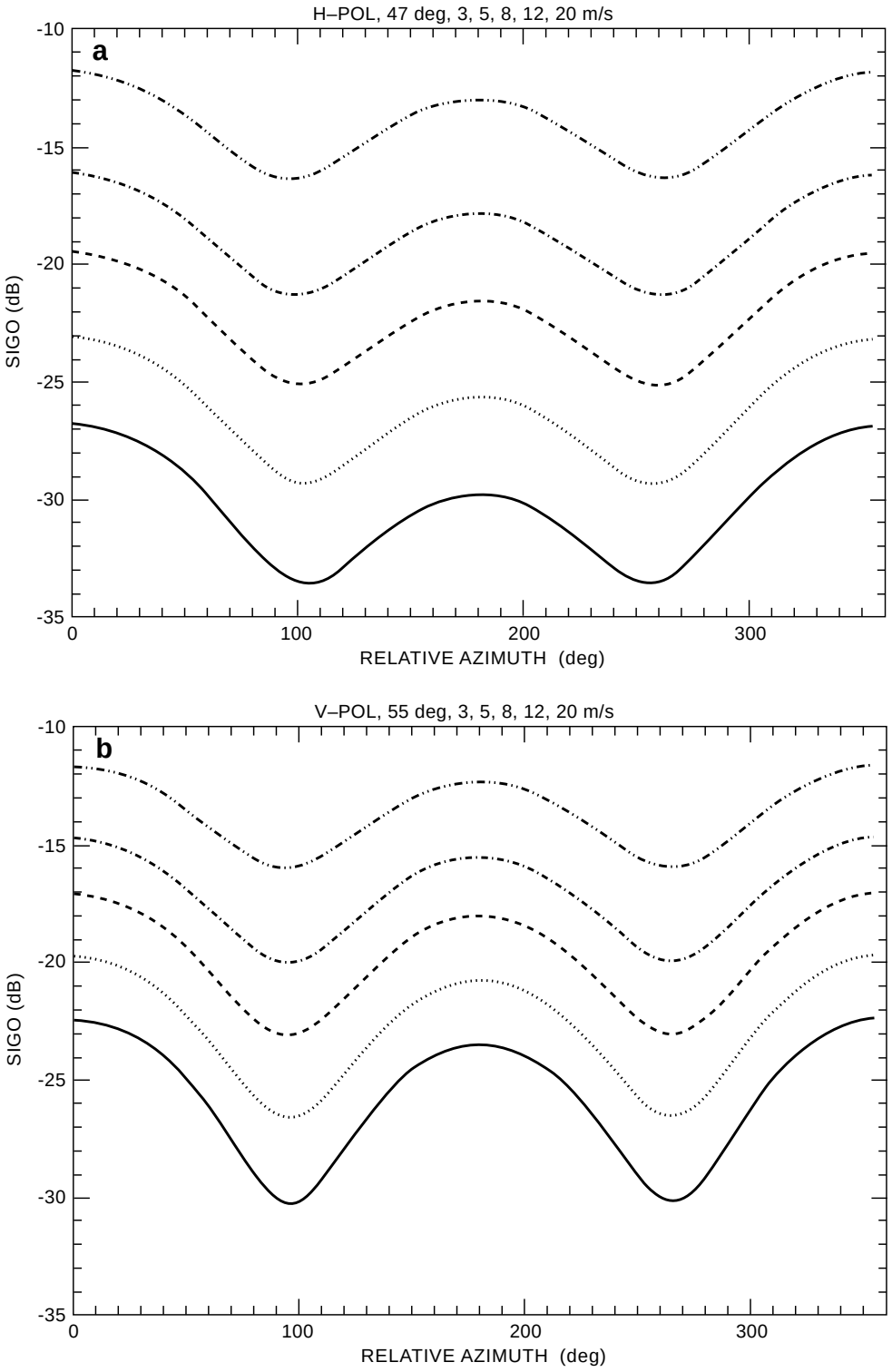


Figure 2. Directional dependences of $\sigma_0$ (dB) as predicted by the SASS-2 model function for wind speeds of 3 (solid), 5 (dotted), 8 (dashed), 12 (dash-dot), and 20 (dash-dot-dot-dot) m/s. (*a*): Inner beam, 47° incidence angle, h-pol; (*b*): Outer beam, 55° incidence angle, v-pol.

upwind-crosswind modulation, the upwind-downwind asymmetry increases with increasing incidence angle, is larger for h-pol than for v-pol, and is largest at low wind speeds.

Insufficient knowledge of the detailed relationship between environmental conditions and sea-surface roughness on scales from millimeters to hundreds of meters, as well as of the mechanisms by which incident electromagnetic radiation is scattered at moderate incidence angles from realistically rough ocean surfaces, precludes derivation of theoretically based model functions. Neither the precise wind velocity dependence of $\sigma_0$ nor its dependences on subsidiary environmental parameters can be described analytically. Although near-power law wind speed dependence (at fixed azimuth and incidence angles) and highly truncated Fourier expansions (ie., $\sigma_0 = A_o + A_1 \cos(\chi) + A_2 \cos(2\chi)$) in direction are often used to approximate the model function, persistent outliers in all existing data sets and cogent mathematical arguments (eg. Donelan and Pierson, 1987; Wentz, 1991) highlight the approximate nature of these functional descriptions. While the SASS-2 model function is the most accurate and consistent Ku-band model presently in existence, the flight of NSCAT and theoretical, laboratory, and field investigations will result in improvements before the flight of SWS.

The software implementation of the model function has a large impact on the generality, speed, and flexibility of the wind retrieval processing. A fully tabular model function representation will be used for processing SWS data, allowing changes to the model function to be made without requiring modification of software or algorithms. In this representation, $\sigma_0$ values are given at regular intervals in $(w, \chi, \theta)$ space. The resolution in parameter space is chosen to be sufficiently fine such that simple linear or quadratic interpolation can be performed with high accuracy between table entries. For NSCAT, resolutions of 1 m/s in speed, 5° in azimuth, and 2° in incidence angle were sufficient for the SASS-2 model function and linear interpolation. However, the NSCAT fan-beam design required specification of the model function over incidence angles from 15° –65° for both polarizations. Higher resolution in incidence angle may be possible for the SWS processing, yielding increased accuracy and computational speed, since the SWS instrument acquires data at only two incidence angles, and at only one polarization for each. It will thus be possible to tabulate the model function for SWS with very high incidence angle resolution near each of the two required incidence angles.

The tabular model function adds significant flexibility to the scatterometer processing. Model function table entries can be modified without changing the processing software or algorithms. New information related to only a small region of parameter space (eg., low wind speed behavior) can be incorporated without altering the entire table. In the event that a fully analytic model function is eventually developed, table entries can be calculated from the analytical form. The tabular model function can also accommodate information that may become available pertaining to the influences of subsidiary (non-wind) geophysical variables, such as sea-surface temperature, through additional table dimensions.

### *2.1.3 Multiple Measurements*

Naderi et al. (1991) illustrate schematically the method by which multiple, colocated measurements of $\sigma_0$ can be combined with the model function to estimate surface wind velocity. The model function defines the locus of wind speeds and directions corresponding to each $\sigma_0$ measurement. In the case of noise-free measurements and perfect knowledge of the model function, intersections of these loci define possible wind velocity solutions consistent with all $\sigma_0$ measurements. If only two colocated $\sigma_0$ measurements from different radar geometries are available, up to four intersections of the loci exist, owing to the near-symmetric oscillatory nature of the model function with respect to direction. Each of these intersections represents a possible wind velocity solution, and is denoted in the scatterometer literature as an "ambiguity." Additional measurements from different geometries reduce the number of intersections and allow estimation of a unique wind velocity in the idealized case. In practice, errors in the $\sigma_0$ estimates and the model function result in "near-intersections"; the upwind-downwind near-symmetry of the model function leads (in general) to two ambiguities with similar speeds and differing in direction by $\sim 180^\circ$ (see section 3.5).

## *2.2 Previous spaceborne scatterometers*

**SKYLAB S-193:** The first western spaceborne scatterometer was the S-193 scatterometer-radiometer instrument that flew on the Skylab mission in 1973. This instrument consisted of a steerable parabolic antenna with associated transmit and receive electronics. It operated at 13.9 GHz, and is described in Young and Moore (1977). The instrument had only a single pencil-beam, and it was not rotated in such a way as to observe backscatter from the same locations on the ocean surface at different viewing geometries.

Thus, only a single observation was typically obtained; independent information on wind direction was required to retrieve wind speed (or vice versa) from S-193 measurements. Nonetheless, the S-193 experiment demonstrated that centimetric backscatter from the ocean could be detected by spaceborne instruments at moderate incidence angles, and that the radar cross-section varied appreciably with both wind speed and relative wind direction. On the whole, however, the data obtained were not generally scientifically useful.

**SEASAT SASS:** The SEASAT-A Satellite scatterometer instrument (SASS) was the first dedicated spaceborne microwave scatterometer. It flew on the SEASAT mission from June-October, 1978, and operated at a frequency of 14.6 GHz. The SASS instrument used 4 fan-beam antennas to illuminate measurement swaths on each side of the spacecraft ground track, with ground footprints oriented at angles of $\pm 45^\circ$ and $\pm 135^\circ$ with respect to the subsatellite track. As only two azimuthal measurements were obtained at each location in the swaths, it was not possible to determine a unique wind direction based on scatterometer data alone. The use of fixed analog Doppler filters to achieve along-beam resolution neglected the (latitude-dependent) contribution of the earth's rotation to the Doppler shift of the backscattered signal. This caused a systematic distortion of the measurement cell geometry with latitude and azimuth angle, yielding different effective swath widths for fore and aft beams and resulting in difficulties colocating the measurements from different beams.

Although there were many difficulties associated with the processing and interpretation of SASS data, the SASS instrument represented a milestone in scatterometer development and a positive scientific contribution to oceanographic and meterological research. The large quantity of accurate backscatter data acquired by SASS at both horizontal ("h-pol") and vertical polarizations ("v-pol"), some in coincidence with conventional surface environmental measurements, allowed development of accurate model functions relating $\sigma_0$ to near-surface winds. The SASS measurements also proved to be an invaluable set of realistic data for the development and testing of wind retrieval and ambiguity removal algorithms (discussed below in sections 3.4 and 3.5). Although the SEASAT data set was temporally short by oceanographic standards, a wide range of scientific studies have been conducted using vector wind information calculated from SASS measurements.

**ERS-1 AMI:** The European Space Agency (ESA) ERS-1 mission was launched in July, 1991, carrying a C-band (5.3 GHz) Active Microwave Instrument (AMI) which operates both as a SAR and as a scatterometer.

In scatterometer mode, the ERS-1 AMI illuminates a 500 km wide swath on the starboard side of the spacecraft. Although fan-beam antennas are used to achieve the broad swath illumination for the AMI as with SASS, the AMI utilizes range gating, rather than Doppler filtering, to achieve along-beam spatial resolution. Within the measurement swath, the ERS-1 AMI illuminates footprints oriented at 45° , 90° , and 135° with respect to the satellite ground track; each location in the swath is therefore imaged from three separate viewing geometries. This "3-look" imaging strategy successfully reduces the 4-fold directional ambiguity to a two-fold ambiguity for most measurements, with directions approximately 180° apart (see Naderi et al., 1991, for a simple illustration). This reduction in directional ambiguity greatly simplifies the processing required to select a single, unique direction consistent with the $\sigma_0$ measurements and the model function.

The ERS-1 AMI has operated nearly continuously since early 1992, and has provided the longest record of global scatterometer data yet obtained. Although its coverage is limited by its single-swath design and narrow swath width and there appears to be a lack of wind velocity sensitivity at C-band (especially at low wind speeds and small incidence angles), the ERS-1 AMI vector wind data are being actively studied by the oceanographic, meteorological, and air-sea interaction research communities. Of particular importance to the algorithm focus of this document, the ERS-1 scatterometer $\sigma_0$ data, with its 3 looks at each location, provides a wide-ranging, realistic test-bed for wind retrieval and ambiguity removal algorithms.

### *2.3 Planned missions prior to the flight of SeaWinds*

Both C- and Ku-band scatterometers will fly in the mid-1990's before the planned launch of the EOS SeaWinds instrument on the ADEOS- II mission. The ERS-2 mission will begin in early 1995 and will carry a 3-look, single-swath, C-band AMI identical to that on ERS-1. The planned overlap between the ERS-1 and ERS-2 missions should allow on-orbit cross-calibration of the two instruments, resulting in a 5-7 year data set of consistent winds from C-band scatterometers.

The NASA Scatterometer (NSCAT) instrument is being implemented as a follow-on to SASS (Naderi et al., 1991). While based heavily on SASS heritage, NSCAT has significant design enhancements that will allow it to obtain more accurate and extensive $\sigma_0$ and vector wind measurements. Like SASS, NSCAT will operate at Ku-band (due to changes in the world allocation of frequency bands, the NSCAT frequency will

be 13.995 GHz), and will use fan-beam antennas to allow $\sigma_0$ measurements to be obtained in two, $\sim$ 600 km wide swaths (defined by incidence angles of approximately $20° - 60°$). NSCAT will fly in a polar orbit as a NASA contribution to the Japanese ADEOS mission, with launch in early 1996 and a planned 3-year mission.

The NSCAT design addresses two of the most important deficiencies identified in the SASS data: NSCAT will have on-board digital Doppler filtering with variable center frequencies and bandwidths in order to allow $\sigma_0$ cells from all antennas to be collocated at every latitude, and the addition of a third antenna azimuth in each vector wind swath will (as in the case of the ERS-1 instrument) provide information which will greatly improve the accurate selection of unique wind directions (simulations indicate that generally two ambiguities, nearly 180° apart, will result from the NSCAT measurements). At each point within the measurement swaths, NSCAT will obtain looks at 3 azimuthal angles (±45°, +65° , -115° , and ±135° relative to the groundtrack). Measurements of vertically polarized $\sigma_0$ will be made at each angle, while additional measurements at h-pol will be obtained at +65° and -115° .

The full NSCAT experiment includes a ground-based data processing system designed to reduce the raw NSCAT and ancillary data to engineering units and to process the data to earth-located $\sigma_0$, vector winds, and temporally and spatially averaged wind field maps. Although some modifications must be made because of differences in instrument design and mission instrument complement between NSCAT and SWS and between ADEOS-I and ADEOS-II, the full specifications and algorithm testbed developed for NSCAT provides the fundamental basis for the SWS algorithms discussed in this document.

### *2.4 SeaWinds Experiment Objectives, Requirements, and Data Products*

#### *2.4.1 Experiment Objectives*

The SeaWinds scatterometer system will be a Ku-band system designed to acquire global measurements of normalized radar cross-section ($\sigma_0$) from which all-weather estimates of near-surface wind velocity will be calculated over the ice-free global oceans. Analyses of the raw $\sigma_0$ measurements will be used for moderate-resolution studies of land and ice surfaces. The vector wind data from SWS will be used, in conjunction with other remotely sensed and conventional data, in a variety of oceanographic, meteorological, and air-sea

interaction studies.

*2.4.2 Mission Requirements*

The high-level mission requirements for the SWS system are detailed in the SWS Science and Mission Requirements Document (JPL, 1994) and are summarized in Table 1.

**Table 1:**

**SWS Key Mission Requirements**

| | |
|---|---|
| Wind Speed Accuracy: | |
| 2–20 m/s | <2 m/s rms |
| 20–30 m/s | <10% rms |
| Wind Direction Accuracy: | <20° rms |
| Wind Cell Resolution: | 50 km (desired)<br>100 km (maximum descope) |
| Radiometric Compensation: | Required for atmospheric attenuation to 95% absorption levels, where AMSR data are available |
| Short-time Coverage: | >90% of ice-free global oceans sampled (to accuracy specifications as above) at least once every 2 days |
| Liftime: | 3 years, 5-year goal |

The SWS mission requirements are similar to those established for NSCAT (JPL, 1988) and represent a realistic merging of oceanographic and meteorological science requirements.

Three changes in the SWS mission requirements relative to the NSCAT requirements should be noted. The NSCAT fan-beam instrument will acquire $\sigma_0$ measurements with nominal 25 km resolution and vector winds will be calculated with $\sim 50$ km resolution by combining adjacent $\sigma_0$ measurements. For a variety of spacecraft accommodation-related reasons, both the raw $\sigma_0$ and the vector wind resolution for SWS will be $\sim 50 - 60$ km.

Although the atmosphere is nearly transparent to Ku-band microwave radiation, it is not perfectly clear – variations in atmospheric liquid water content and precipitation-induced roughness on the sea surface modify the apparent radar cross-section of the ocean measured by satellite-borne instruments. As discussed

more fully in section 3.3, data from multi-channel microwave radiometers colocated with scatterometer $\sigma_0$ measurements can be used to estimate atmospheric attenuation at the scatterometer frequency, thus allowing the scatterometer $\sigma_0$ measurements to be corrected for atmospheric attenuation effects and improving the scatterometer wind velocity estimates. Data obtained by the NSCAT instrument on the ADEOS-I mission will not be correctable, as there will be no microwave radiometer data colocated in time and space with the NSCAT measurements. However, the AMSR instrument, a multichannel microwave radiometer on the ADEOS-II spacecraft, will obtain nearly colocated brightness temperature data at a variety of frequencies; the SWS mission requirements have been modified from those of NSCAT to require the SWS $\sigma_0$ measurements to be corrected for atmospheric attenuation whenever sufficient AMSR data are available.

Finally, wind velocity accuracy requirements for NSCAT were stated in terms of speed and direction errors for the ambiguity closest to the true wind direction, thus effectively decoupling the instrument performance and wind retrieval processing from the accuracy of the ambiguity removal processing. Both simulations based on the NSCAT and SWS baseline designs and experience with the ERS-1 scatterometer data suggest that highly accurate ambiguity removal algorithms can be developed for scatterometers that acquire 3 or more azimuthal "looks" at most locations within the measurement swath. The SWS accuracy requirements have been applied to the *chosen*, rather than the closest, ambiguity; velocity accuracies for SWS thus apply to the full hardware/software system.

### *2.4.3 SWS Processing Overview and Standard Data Products*

Significant processing is required to calculate earth-located $\sigma_0$ and ocean vector winds from the raw SWS data. However, as scatterometers in general and SWS in particular are designed specifically to allow calculation of ocean vector wind measurements, the processing follows a single path, rather than breaking into multiple branches as is common with several other EOS instruments. The overall processing approach is shown schematically in figure 3, with particular emphasis on the standard data products.

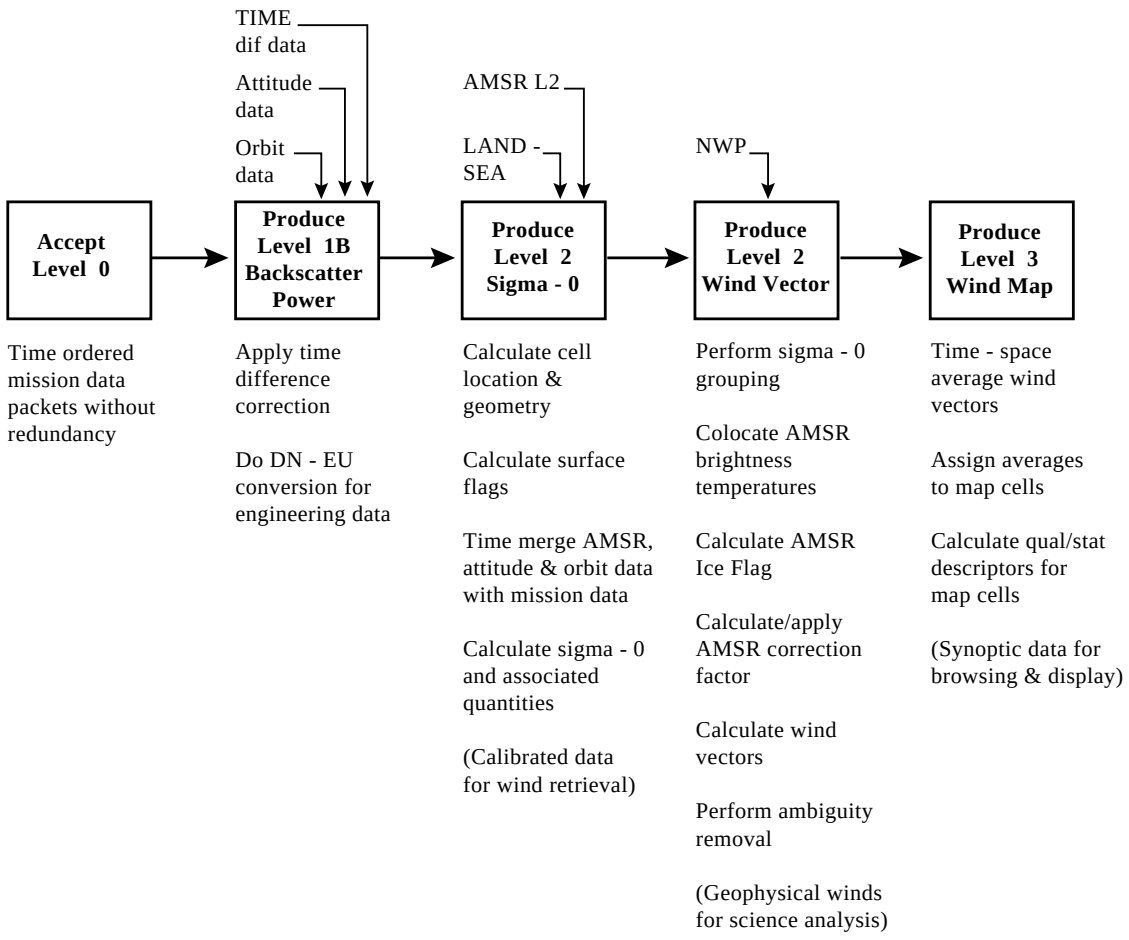


Figure 3. SeaWinds processing flow schematic.

**Level 1B:** The SWS Level 1B standard data product includes all SWS Level 0 raw data, in time order and organized by "SWS Instrument" data orbital revolution (south pole to south pole). SWS data are converted from telemetry units (as in Level 0) to engineering units. Ancillary data include Payload Correction Data, and spacecraft attitude and ephemeris. Time difference corrections are applied, and the spacecraft attitude/orbit data are time merged with SWS instrument data.

While standard definitions define orbits typically by ascending or descending node times, scatterometer processing often operates simultaneously on data obtained at different times (thus associated with different satellite nadir locations). Examples include spatial colocation of $\sigma_0$ measurements obtained from different

viewing geometries and ambiguity removal. If the standard node-to-node definition of an orbit is used, scatterometer processing inevitably requires operations on data from multiple, consecutive orbits. However, these potential multi-orbit calculations are encountered in algorithms which are performed only on open-ocean data. As the continent of Antarctica covers the entire south polar region, it was decided for the NSCAT and SWS processing to take as the basic unit of data the "orbital revolution" defined between southernmost latitudes of the spacecraft nadir point. In the near-polar ADEOS-I and -II orbits, this definition effectively decouples data from consecutive orbital revolutions and provides a natural granularity for the subsequent data processing.

**Level 2: Global Backscatter Cross-sections:** The global backscatter cross-section product is the lowest-level geophysical product from the SWS system. The product consists of time-ordered, global (ice, land, and ocean), earth-located $\sigma_0$ measurements and associated incidence angle, azimuth angle, and radar information (such as $K_p$ ) calculated from the Level 1B backscattered power with quality and surface (land) flags. Ancillary data include earth-located AMSR brightness temperatures (Level 2) at 6.6, 10.65, 18.7, 23.8, and 36.5 GHz at both horizontal and vertical polarizations (supplied by NASDA/ADEOS-II). This data set contains all data necessary to colocate the $\sigma_0$ cells, flag measurements contaminated by sea ice, correct the ocean $\sigma_0$ measurements for atmospheric effects, and calculate sets of directionally ambiguous vector winds.

Grouping of spatially colocated open ocean $\sigma_0$ measurements and colocation of ocean $\sigma_0$ with AMSR data for attenuation correction and rain flagging of ocean $\sigma_0$ cells will be performed as part of the wind retrieval processing. The grouping and colocation processes are extremely efficient if all earth-located data are assigned coordinates in a fixed, regular along-track/cross-track grid centered in the spacecraft nadir track, as described in Dunbar et al. (1988). Assignment of grid coordinates is efficiently performed in conjunction with earth location processing. The Level 2 Global Backscatter Cross-section data and ancillary AMSR data thus will be assigned along-track/cross-track coordinates in addition to latitude/longitude coordinates.

Although vector winds are retrieved only from open-ocean $\sigma_0$ measurements, recent analyses have demonstrated that SEASAT SASS and ERS-1 $\sigma_0$ data acquired over land and ice can be used for a variety of geophysical studies, including ice boundary location, ice typing, and vegetation mapping. The full, global $\sigma_0$ data set thus is expected to have utility beyond retrieval of ocean near-surface vector winds; the

Level 2 $\sigma_0$ data set includes all SWS information required to conduct further geophysical studies.

**Level 2 Vector Winds:** This data set consists of near-surface vector winds over the open ocean within the measurement swath of the SWS instrument. Winds are calculated from spatially colocated, corrected $\sigma_0$ measurements from the Level 2 backscatter cross-section product. Only open-ocean $\sigma_0$ cells (no ice or land contamination) are used in the calculations. Up to 4 ambiguous velocities are reported, in order of descending probability (as calculated by the wind retrieval processing). The single ambiguity chosen by the ambiguity removal scheme is indicated by a flag. Interpolated surface velocities calculated from operational meteorological forecast/analysis data, used to initialize the ambiguity removal algorithm, are included in this data set, as are various quality flags.

*2.5 SeaWinds Flight Instrument*

The SWS flight instrument is a conically scanning, dual pencil beam scatterometer that will operate at 13.402 GHz and will fly as a NASA-supplied instrument on the ADEOS-II mission scheduled for launch in 1998. Key characteristics of the ADEOS-II mission are summarized in Table 2.

**Table 2:**

**Key ADEOS-II Mission Characteristics**

| | |
|---|---|
| Orbit: | 802.9 km altitude<br>98.62° inclination<br>sun-synchronous<br>57-orbit repeat (3.998 day)<br>10:30 AM asc. node |
| Launch Date: | 2/99 |
| Planned Instruments: | GLI (Visual, SW, and thermal IR imager)<br>AMSR (multi-channel microwave radiometer)<br>SWS (13.4 GHz scatterometer)<br>possible others chosen in response to NASDA AO |
| Mass: | 3,500 kg (1,200 kg payload) |
| Power: | 5.0 kW (1.2 kW payload) |

The SWS instrument will be the first scanning pencil beam scatterometer to be flown in space; as noted above, the SASS, ERS-1/2, and NSCAT scatterometers were all fan-beam designs, and the pencil-beam S-193 instrument was not employed as a dedicated scatterometer. While building on the Ku-band heritage of the SASS and NSCAT flight instruments, the SWS scatterometer will be capable of acquiring $\sigma_0$ and vector wind measurements with significantly greater scientific utility than previous Ku-band instruments.

Although a full description of the SWS flight instrument is beyond the scope of the present document, important aspects of the instrument design are summarized in Table 3 and discussed briefly below, with particular emphasis on those aspects of instrument design, performance, and operation that impact directly on the algorithms used to process the raw data to $\sigma_0$ and vector winds.

**Table 3:**

**SeaWinds Key Parameters**

| | |
|---|---|
| Radio Frequency: | 13.402 GHz |
| Transmission Power: | 110 W |
| Pulse Duration: | 1.5 ms (CW or 40 kHz bw FSK) |
| PRF: | ∼192 Hz (commensurate with scan period) |
| | |
| Antenna Aperture: | ∼1 m |
| Antenna Gain: | >39 dB (1-way) |
| Look Angles: | 40°, 46° |
| Incidence Angles: | 47°, 55° |
| Polarization: | h-pol (inner), v-pol (outer) |
| Scan Rate: | 16–20 rpm (chosen pre-launch) |
| Footprint Area: | 30 × 35 km (from 2-way pattern) |
| Swath Width (full): | 1414 km (inner), 1800 km (outer) |

The concept of a scanning pencil-beam scatterometer was first published by Kirimoto and Moore (1984; see also Naderi et al., 1991). Whereas fan-beam scatterometers use a number of fixed, fan-beam antennas with constant orientation relative to the spacecraft velocity vector to acquire multiple backscatter measurements as the satellite orbits, the SWS scanning pencil-beam design uses a spinning parabolic antenna with two transmit and receive feeds to sweep out helical patterns on the earth's surface, as shown in figure 4. By coordinating the instantaneous illuminated pattern on the earth, the pulse repetition rate, and the antenna spin rate, each beam can be used to acquire a spatially contiguous set of $\sigma_0$ measurements.

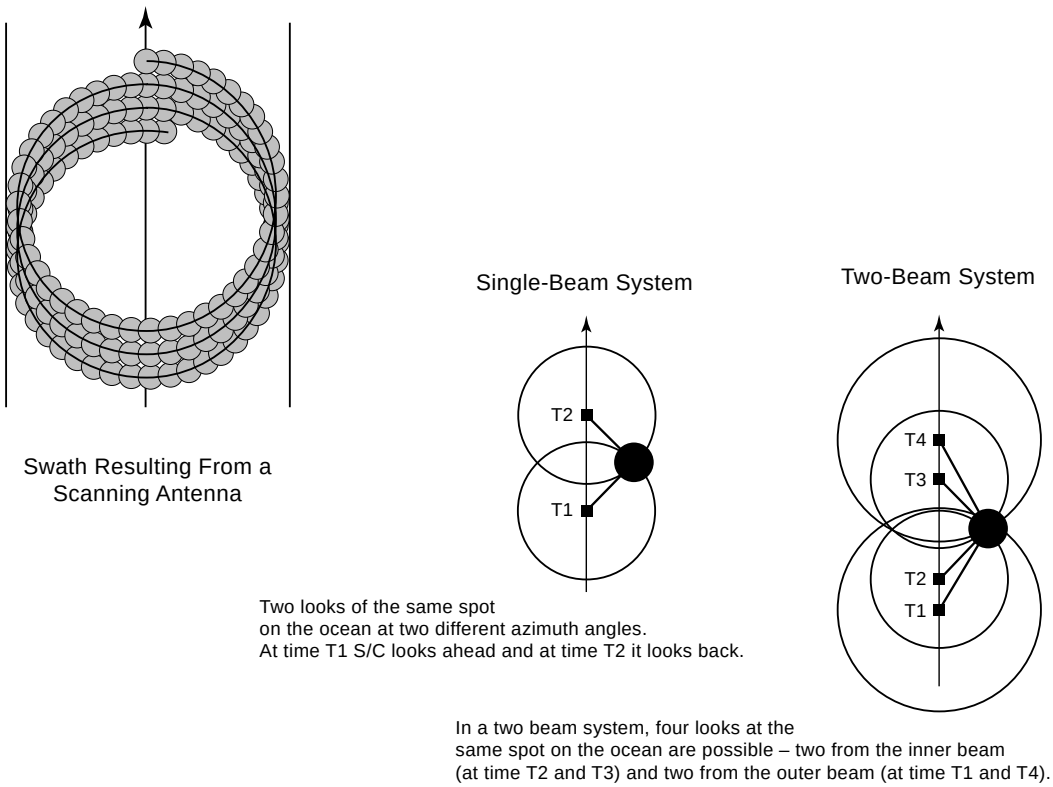


Figure 4. Schematic representation of the SeaWinds scan pattern.

Scanning pencil-beam designs have several inherent advantages over the fan-beam approach used for earlier scatterometers. As all measurements are acquired at two fixed incidence angles, $\sigma_0$ is sensitive to wind velocity at all cross-track locations within the measurement swath. In principle, therefore, the nadir gap present in all fan-beam designs can be eliminated. (However, the set of azimuth angles over which the $\sigma_0$ measurements are acquired *is* a function of cross-track location, and thus the accuracy of the wind velocity solutions can vary systematically with cross-track distance.) Both the incidence angles and polarizations of the inner and outer beams can be optimized to assure high directional modulation of $\sigma_0$ while preserving sufficient signal-to-noise ratios. Finally, the empirical model function needs to be known only near the two incidence angles corresponding to the inner and outer beams, rather than over the broad range from $\sim 15°$–$65°$ required for fan-beam instruments.

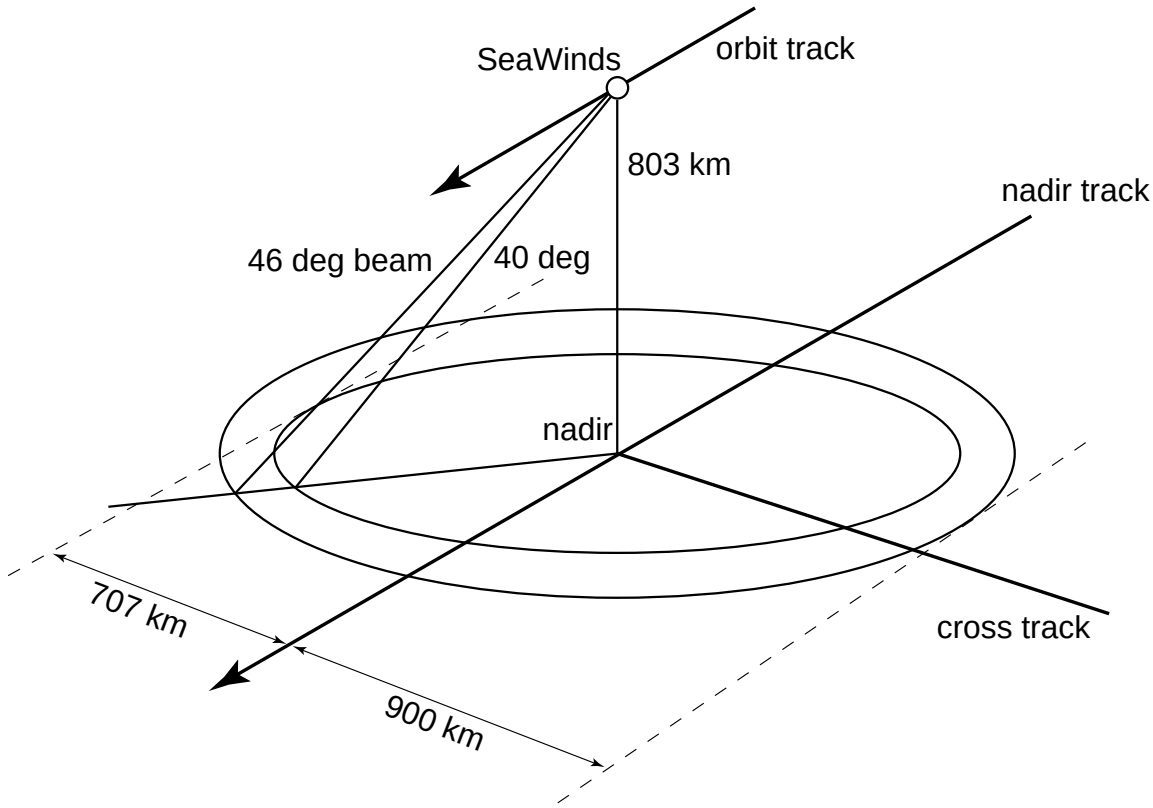


Figure 5. Schematic representation of the SeaWinds measurement geometry.

The measurement geometry for SWS is shown in figure 5. A single, $\sim$ 1 m diameter parabolic dish antenna will rotate at $\sim$ 18 rpm to provide the basic scanning. Offset feeds generate transmitted and received beams with look angles of 40° and 46° (measured at the spacecraft with respect to nadir). At the nominal orbital altitude of 803 km, the two beams trace out near-circles on the earth's surface with radii of $\sim$710 and 900 km; owing to the curvature of the earth, the incidence angles at the surface are 47° and 55° for the inner and outer beams. Beamwidths are 1.6° x 1.8° (elevation x azimuth) for the inner beam, and 1.4° x 1.7° for the outer beam. The instantaneous illuminated area on the surface (measured with respect to the -3 dB points in the 2-way antenna gain patterns) is elliptical with characteristic dimensions of 30 x 35 km for both beams.

At cross-track distances $<$ 707 km (the radius of the inner beam), measurement cells are sampled from four geometries: first by the outer beam looking ahead of the spacecraft; next by the inner beam, looking

ahead (and later behind) the subsatellite point; and finally again by the outer beam, looking behind. At larger cross-track distances, only two measurements are obtained, both by the outer beam. This results in a much different sampling geometry than is obtained from fan-beam scatterometers such as NSCAT or ERS-1. Even at small cross-track distances, the SWS $\sigma_0$ measurements are sensitive to wind velocity, as the *incidence angles* of the two beams are constant and large, independent of cross-track distance. However, as shown in figure 6, the azimuth angles (relative to the spacecraft nadir track) vary with cross-track distance. For fan-beam scatterometers, the relative azimuths of the measurements are constant at all locations in the swath, although the incidence angles at which the measurements are obtained vary systematically across the swath.

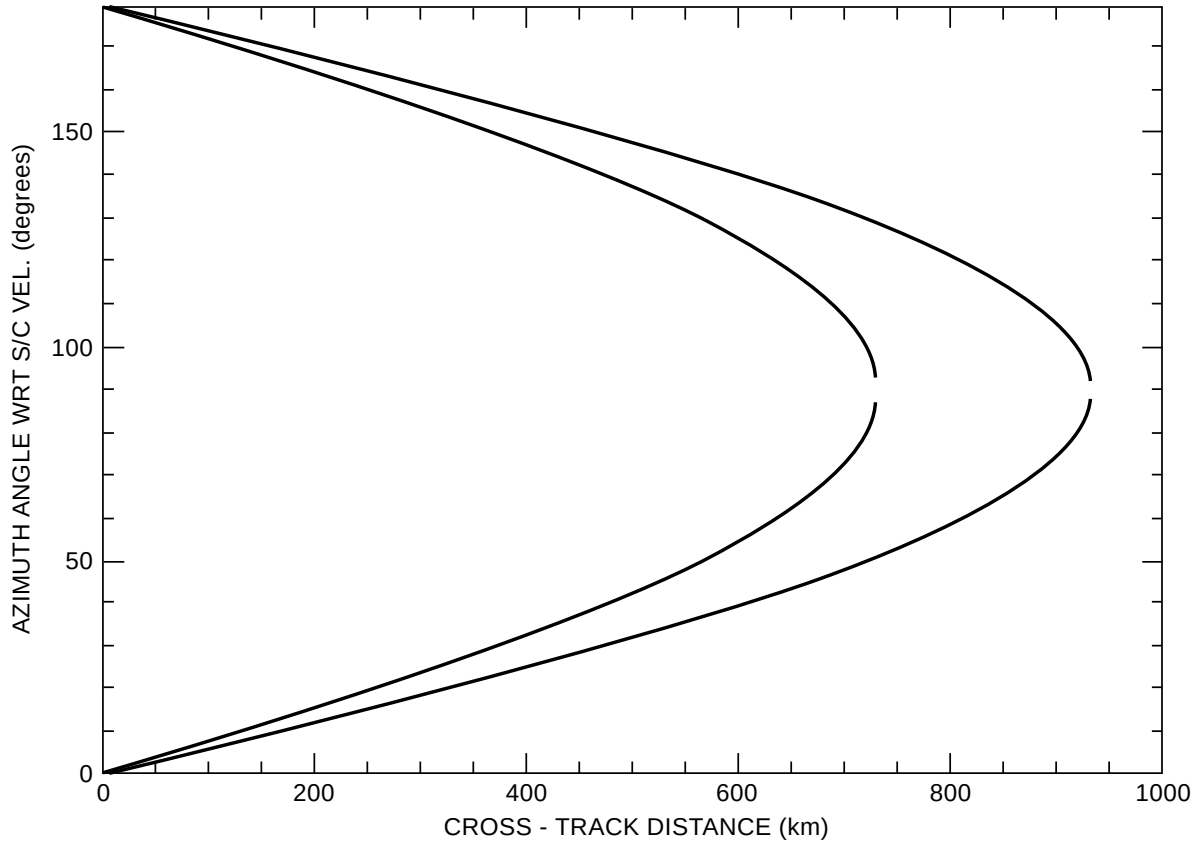


Figure 6. Azimuth angles vs. cross-track distance for the SWS measurement geometry shown in figure 5. Azimuth angles (degrees) are relative to the spacecraft velocity vector.

The pulse repetition frequency (PRF) and antenna rotation rate are chosen to be compatible with the

orbital velocity of the spacecraft and the instantaneous illumination pattern of the antenna. At the 18 rpm rotation rate, each full rotation ("scan") requires 3.33 seconds; in that period, the spacecraft has moved ∼22 km in the along-track direction. Illuminated 30 x 35 km cells from consecutive scans thus overlap in the along-track direction, assuring that that there are no along-track gaps in the measurement swath.

The SWS transmits 1.5 ms pulses of modulated CW radiation with a PRF chosen such that the scan period and the PRF are commensurate. This assures that pulses will be transmitted at the same azimuthal locations in each scan. For an antenna rotation rate of 18 rpm and a PRF of 192 Hz, there are 640 pulses/scan (340 for each beam). The resulting ∼1° azimuthal resolution translates to ∼ 14 and ∼ 17.6 km azimuthal spacing between cell centers in the inner and outer beams, respectively. There is thus significant overlap between $\sigma_0$ measurement cells in both the along-track and cross-track dimensions; the entire measurement swath is fully covered. Calculation of scatterometer wind velocities requires spatially colocated $\sigma_0$ measurements, and as discussed below in section 3.4, the SWS $\sigma_0$ data are grouped into 50 x 50 km cells in an along-/cross-track grid for wind retrieval. The scanning geometry/timing outlined above results in approximately 6 (at the satellite subtrack) to 30 (at the far edges of the swath) $\sigma_0$ measurements whose centers fall within the 50 x 50 km wind vector cell grid.

The PRF of ∼ 192 Hz corresponds to transmit/receive cycle periods of ∼ 5.2 ms. A pulse is transmitted from one beam (either the inner or the outer) at the start of the transmit/receive cycle. Typical 2-way travel times are ∼ 0.00733 and 0.00748 seconds for the inner and outer beams, respectively. Following pulse transmission, the remaining time in each cycle is used to receive the pulse that was transmitted in the *previous* cycle. The continuous scanning of the antenna causes it to have rotated ∼ 0.8° (approximately half of the beamwidth) between the midpoint of the transmit pulse and the midpoint of the received pulse. Separate patterns for the transmit and receive antenna gains must thus be used when evaluating the radar equation to calculate $\sigma_0$ (see section 3.2). The next pulse is transmitted from the other beam, and the process repeats alternately.

The received power is composed of both backscattered power from the transmit pulse and noise from natural emissivity from the earth-atmosphere system at the SWS frequency. Accurate calculation of the $\sigma_0$ of the earth's surface requires estimation and subtraction of the noise power. The SWS instrument

simultaneously estimates the total (signal plus noise) power and the noise power by passing the received signal through two filters.

The total power (signal plus noise) detection scheme isolates the returned signal in both time (through range gating) and frequency (through Doppler filtering). Although the transmitted pulse is a nearly pure tone, the backscattered signal is spread and Doppler shifted as a result of the satellite velocity and the earth's rotation. The center frequency of the returned pulse is therefore a function of both the orbit position and the antenna azimuth. The Doppler shift varies over a range of $\pm$500 kHz. The Doppler filter is a fixed bandwidth ($\sim$80 kHz), tunable filter with center frequency set by the SWS instrument based on antenna azimuth and spacecraft orbit location information. The output of the Doppler filter is integrated over a time period corresponding to the expected arrival time of the backscattered pulse. The delay time between the transmission of the pulse and the opening of the range gate depends primarily on the total 2-way flight time, which in turn is a function of the selected beam and spacecraft orbit position (which together dictate the slant range).

The purpose of the noise filter measurement is to estimate the total noise power contribution to the integrated output of the Doppler echo filter. This is accomplished by integrating the output of a wide ($> 1$ MHz) fixed bandwidth filter over the same period for which the echo range gate is open. The noise filter passband includes all possible center frequencies for the returned pulse.

The SWS incidence angles and signal polarizations are chosen to optimize wind measurement performance, coverage, and spatial resolution. As noted in the model function discussion, the wind speed sensitivity, upwind-crosswind modulation, and upwind-downwind asymmetry all increase with increasing incidence angle. Large incidence angles also result in wide measurement swaths, increasing spatial coverage. At the same time, however, absolute cross-sections decrease with increasing incidence angles, as does spatial resolution (given a fixed antenna gain pattern). In addition, although directional modulations are typically larger for h-pol than for v-pol radiation, cross-sections are lower. This problem is solved for SWS by making the inner beam h-pol and the outer beam v-pol.

## 3. Algorithm Descriptions

### *3.1 Algorithm Design and NSCAT Heritage*

A complete ground processing system has been developed for the Ku-band NSCAT Scatterometer. As part of this development, all algorithms were fully specified and reviewed by the NSCAT Science Team as well as Project personnel and outside experts. A full software testbed was constructed. This testbed, with extremely minor modifications, is being used operationally to process the ERS-1 data from $\sigma_0$, through wind retrieval and ambiguity removal. Although NSCAT antenna azimuths, beam polarizations, and (especially) basic frequencies are different from those for the C-band, 3-stick, single-swath ERS-1 scatterometer, the flexible design of the wind retrieval and ambiguity removal portion algorithms in the testbed allows it to be used to process the ERS-1 scatterometer data with only trivial modifications. The SWS algorithms are based heavily on the NSCAT algorithms, with modifications only as necessary to accommodate changes in instrument characteristics (as described in section 2.5) or data availability (as in the case of the atmospheric attenuation correction to $\sigma_0$ using AMSR radiometer data, described in section 3.3). The theoretical bases for $\sigma_0$ calculation using both signal+noise and noise-only measurements, the maximum likelihood approach to wind retrieval, and the basic circular median filter approach to ambiguity removal are all common to the NSCAT, as well as SWS, processing.

### *3.2 $\sigma_0$ calculation*

Objective: The objective of the $\sigma_0$ calculation algorithm is to calculate the earth-located, apparent normalized backscatter cross-section of the earth-atmosphere system (and associated quantities required in wind retrieval processing) based on the measured signal plus noise and noise-only power measurements acquired by the SWS instrument.

Background: Earth-located global estimates of normalized radar cross-section ($\sigma_0$) are the lowest-level SeaWinds data products of direct geophysical utility. The cross-section estimates are based fundamentally on the integrated power measurements contained in the Level 1B SWS product, but also utilize ancillary spacecraft attitude and position data, instrument pointing and calibration data, instrument tables (such as antenna gain calibrations), and fixed land-sea-ice tables. Computations are performed for each cell of

each of the two SWS conically scanned beams for which Level 1B received power data exist. Outputs of this set of algorithms make up the Level 2 $\sigma_0$ data product and include calculated signal and noise powers (watts), signal-to-noise ratio, system gain from ground-based calibration tables and on-board calibration measurements, and the "apparent" normalized radar cross-section of the earth at the cell location. Note that the "apparent" $\sigma_0$ estimate is not corrected for the effects of atmospheric attenuation (see section 3.3).

Many of the calculations (eg., earth-locating, land/sea flagging, etc.) are straightforward and do not require exposition of their theoretical bases. Others, such as the calculation of certain coefficients for $K_p$ , are highly complex, well-documented (eg., Long, 1993), and are ultimately reduced to table lookups in the final algorithms. They, too, are not described here. What is of primary focus is the method by which the measured backscattered powers are processed to yield estimates of $\sigma_0$.

Physical Basis: The radar equation (eg., Ulaby et al., 1986) describes the fundamental relationships between characteristics of the radar, scattering properties of the surface, and the transmitted and received powers. The radar equation for an essentially monostatic radar (such as SWS) and a point target is:

$$P_b = \frac{P_t G_t G_r \lambda^2 L \sigma_0}{(4\pi)^3 R^4} \qquad (3.2-1)$$

where $P_t$ and $P_b$ are the transmit and backscattered powers, respectively; $G_t$ and $G_r$ are the transmit and receive one-way antenna gains (gains are different owing to antenna rotation between the time that a pulse was transmitted and the time it is received); $\lambda$ is the radar wavelength; $R$ is the slant range (assumed equal for transmit and receive); $L$ represents overall system losses; and $\sigma_0$ is the normalized radar cross-section.

The SWS received power measurements are acquired from cells on the earth's surface that are several tens of kilometers in characteristic dimension. Therefore, each cell contains a very large number of individual scatterers, each of which has characteristic dimension of centimeters to meters. In principle, therefore, the applicable radar equation is a generalization of (2) formed by integrating the point scattering equation (1) over the entire illuminated area:

$$P_b = \frac{P_t L \lambda^2}{(4\pi)^3} \iint \sigma_0 \frac{G_t(x,y) G_r(x,y) F(x,y)}{R^4(x,y)} \, \mathrm{d}x\mathrm{d}y \qquad (3.2-2)$$

where $F$ is the equivalent signal filter gain over the measurement area. The integral must be evaluated over the entire surface of the earth illuminated by the transmit and receive antenna patterns; in practice,

the narrow pencil beam antenna pattern (small amplitude sidelobes) allows the domain of the integral to be restricted to only the area on the ocean falling within the −3 dB contour of the (2-way) antenna gain pattern.

It is clear from (3.2-2) that two calculations are required to estimate $\sigma_0$ from the measured receive powers in the Level 1B product: (1) estimation of *backscattered* power $P_b$ from the measured *total* (backscattered + noise; $P_r$) and noise-only power ($P_n$) in the Level 1B product; and (2) calculation of $\sigma_0$ by evaluating equation (3.2-2).

#### *3.2.1.1 Estimation of $P_b$*

The total received power $P_r$ at the scatterometer consists of backscattered radiation $P_b$ from the transmitted pulse and a contribution $P_n$ resulting both from the natural emissivity (in the scatterometer receive frequency band) from the earth-atmosphere system and additional noise introduced by the instrument electronics:

$$P_r = P_b + P_n. \qquad (3.2-3)$$

An estimate of $P_n$ must thus be subtracted from $P_r$ before the apparent $\sigma_0$ of the surface can be calculated.

As discussed in section 2.5 above, the SWS system acquires simultaneous measurements of received power over two frequency bands: a narrow (∼80 kHz) band centered on the expected Doppler-shifted frequency of the returned pulse, and a broad, fixed (> 1 MHz) band containing the backscattered signal frequencies. Both measurements are limited in time by a narrow range gate centered on the expected return time of the transmitted pulse, thus further minimizing extraneous noise.

As shown by Spencer (1994), the expected value of the integrated received power is given by

$$P_b = (P_r - \alpha P_n) / \left[ \int G_d(f) s(f) \mathrm{d}f - \alpha \int G_n(f) s(f) \mathrm{d}f \right], \qquad (3.2-4)$$

where $\alpha$ is thus the ratio of the effective "signal" and "noise" filter bandwidths; $\alpha = \int G_d(f)\mathrm{d}f / \int G_n(f)\mathrm{d}f$. In equation (3.2-4), $P_r$ and $P_n$ are the integrated "received" and "noise" power measurements from the Level 1B product, $G_d(f)$ and $G_n(f)$ are the frequency-dependent gains through the instrument Doppler- and noise-filter signal paths, respectively, and $s(f)$ is the normalized shape function for the returned signal spectrum ($\int s(f)\ \mathrm{d}f = 1$).

It must be emphasized that (3.2-4) is an equation for the *expected* value of $P_b$, as it has been assumed in the derivation of (3.2-4) that the noise power spectrum is white over the entire frequency range of the noise filter. The actual measured values of $P_r$ and $P_n$ are (essentially independent) realizations of random variables, and thus are not identically equal to their expected values. The *estimated* $P_b$ can assume (unphysical) negative values, especially when the signal-to-noise ratio is small. As noted in section 3.4, wind retrieval algorithms must accommodate such negative $P_b$ estimates.

#### *3.2.2.2 Calculation of $\sigma_0$*

Although (3.2-4) can be used to estimate $P_b$ from $P_r$ and $P_n$ measurements from each cell, the large-area radar equation (3.2-2) cannot be evaluated directly. As discussed in Dunbar et al. (1988), (3.2-2) can be further simplified by assuming that $\sigma_0$ is constant over the cell area $A_c$ (the effective domain of the integral in (3.2-2)), yielding

$$\sigma_0 = P_b \left[\frac{P_t L \lambda^2}{(4\pi)^3}\right]^{-1} \left[\iint \frac{G_t G_r F}{R^4} \mathrm{d}A\right]^{-1}. \qquad (3.2-5)$$

The mean value theorem of calculus is then used (Dunbar et al., 1989) to rewrite (3.2-5) as

$$\sigma_0 = P_b \left[A_c P_t \left(\frac{G^* \lambda}{4\pi R_o^2}\right)^2 \frac{L}{4\pi}\right]^{-1} \Lambda(G, A_c, R_o), \qquad (3.2-6)$$

where $G^*$ and $R_o$ are peak antenna gain and slant range to the center of the cell, respectively, and $\Lambda(G, A_c, R_o)$ is the weighting function

$$\Lambda = A_c R_o^4 G^{*2} \left[\iint G_r G_t F R^{-4} \mathrm{d}A\right]^{-1}. \qquad (3.2-7)$$

Importantly, the only dynamic variable in the areal integral on the RHS of (3.2-7) is the slant range $R$. Detailed tables of the integral can thus be calculated, stored, and utilized in the calculations based on the known antenna and filter gains $G$ and $F$.

### *3.3 $\sigma_0$ Atmospheric Correction*

Objective: The objective of the $\sigma_0$ correction algorithm is to correct (where possible) the apparent $\sigma_0$ measurements of the ocean-atmosphere system by subtracting non-wind effects related to anomalous attenuation and scattering of the microwave signal as it propagates through the atmosphere. The algorithm should

identify high rainfall conditions for which correction of the $\sigma_0$ measurements is not possible, and flag such contaminated $\sigma_0$ cells.

Background: Although the atmosphere is generally considered to be extremely clear at Ku-band scatterometer frequencies (13.4 – 14.6 GHz), it is not perfectly transparent. A small amount of Ku-band radiation is absorbed by gaseous $O_2$ and water vapor, and is absorbed and scattered by liquid water present as clouds and rain. Atmospheric modifications to the strength of the transmitted and returned scatterometer pulses are manifested as changes in the apparent $\sigma_0$ of the earth-atmosphere system (see section 3.2). Calculation of near-surface wind velocity from scatterometers is based fundamentally on the assumption that variations in measured $\sigma_0$ (given fixed viewing geometry) are the result of changes in the surface geometry of the sea. It is thus important to identify and correct (if possible) $\sigma_0$ estimates that are corrupted by atmospheric effects not related to the near-surface wind, before the $\sigma_0$ measurements are used to calculate wind velocity. Atmospheric attenuation in cloudy to moderate rain conditions can be estimated indirectly from spatially and temporally colocated brightness temperature measurements obtained by multi-channel microwave radiometers.

Rain flagging and attenuation correction using radiometer measurements was attempted for portions of the SEASAT SASS measurement swaths that were also sampled by the SEASAT SMMR instrument (Moore et al., 1982; Boggs, 1982; Moore et al., 1983). However, the low (and variable with frequency) resolution of the SMMR measurements relative to the SASS backscatter cell sizes, and difficulties associated with SMMR-SASS colocation and partial beam filling resulted in highly uncertain corrections and probable underpredictions of rain rate and flagging (Moore et al., 1983). In any event, the SMMR measurements covered only the starboard SASS swath; no radiometer data were available to attempt flagging/correction of the SASS port swath data. In addition, the SMMR measurements were acquired at a fixed incidence angle of 49° , while the fan-beam SASS data were acquired over a range of incidence angles from 20–65° . The radiometer measurements were thus not taken through the same atmospheric path as the SASS signal, and thus incidence-angle corrections were required.

Rain flagging and $\sigma_0$ correction using radiometer data are presently being carried out as part of the TOPEX/POSEIDON data processing. A nadir-looking microwave radiometer, TMR (a modified version of

the SMMR acquiring measurements at 18, 21 and 37 GHz) allows colocation of radiometer and altimeter data (although there remains a resolution mismatch) and assures that the two instruments are viewing essentially the same atmospheric path. Although the primary altimeter interest is in path delay due to atmospheric water vapor, attenuation corrections and rain flagging are also applied to the altimeter $\sigma_0$ measurements prior to their use for calculation of wind speed.

AMSR Description: Upwelling brightness temperatures from the earth-atmosphere system can be calculated from AMSR measurements. The AMSR multi-channel microwave radiometer onboard ADEOS-II will be a japanese-supplied instrument, and is one of the primary ADEOS-II sensors. $T_B$ data will be obtained for both h-pol and v-pol at frequencies of 6.6, 10.65, 18.7, 23.8, and 36.5 GHz at a nominal incidence angle of 49°. The AMSR will have a single antenna, yielding spatial resolutions of approximately 62, 38.5, 22, 17.2, and 11.2 km at each of the aforementioned frequencies. The 49° incidence angle corresponds to the minimum minmum sensitivity to surface emissivity and reflectivity (Moore et al., 1982; Wentz, 1983) and is similar to the SEASAT-SMMR incidence angle. The AMSR frequencies of 6.6, 10.65, and 36.5 GHz are virtually identical to those used for SMMR, and the AMSR 18.7 GHz frequency is similar to the SMMR and SSM/I channels at 18 GHz. The AMSR measurement at 23.8 GHz is designed primarily to measure water vapor, which has a spectral peak at 22.235 GHz. The 23.8 GHz measurement for AMSR is comparable in frequency location (with respect to the water vapor line) to the 21 GHz SMMR and SSM/I channels, although the SMMR and SSM/I channels lie below the water vapor peak, while the AMSR channel lies above it in frequency). The AMSR channels at 36.5, 23.8, and 18.7 GHz are critical to the calculation of the atmospheric modification to the Ku-band scatterometer signal, as they are primarily sensitive to water vapor (23.8 GHz) and liquid atmospheric water (36.5 and 18.7 GHz); although algorithms designed for SMMR and SSM/I radiometers will be able to be used, exact coefficients will require recalculation due to the frequency differences between the AMSR and previous spaceborne radiometers.

Physical Basis: Ku-band radiation propagating through the atmosphere is attenuated due to resonant absorption by gaseous $O_2$ and water vapor, and to scattering and absorption by liquid water present as clouds and rain. Detailed discussions of these mechanisms and effects are found in the standard texts by

Ulaby et al. (1981), Stewart (1985), and Maul (1986). The total modification to a microwave signal at frequency $f$ due to atmospheric effects at height $z$ can be represented by

$$\alpha_{TOT}(f,z) = \alpha_{O_2}(f,z) + \alpha_{H_2O}(f,z) + \alpha_{CLOUD}(f,z) + \alpha_{RAIN}(f,z) = \alpha_{GAS}(f,z) + \alpha_{LIQ}(f,z), \quad (3.3-1)$$

where the $\alpha$ terms are given in units of db/km. The transmissivity of the atmosphere at frequency $f$ is then

$$\tau(f) = \sec\theta \int_0^H \alpha_{TOT}(f,z)\mathrm{d}z \quad (3.3-2)$$

where $\theta$ is the look angle relative to nadir and $\sec\theta$ accounts approximately for the increased path length due to off-nadir viewing, and $H$ is the effective height of the atmosphere over which significant modification takes place (typically 20-30 km). The corrected $\sigma_0$ of the sea surface in dB (without *any* atmospheric effects) is given simply by

$$\sigma_{0COR} = \sigma_{0MEAS} + 2\tau(f), \quad (3.3-3)$$

and $\sigma_{0COR}$ and $\sigma_{MEAS}$ are the corrected and measured normalized radar cross-sections.

Precise calculation of gaseous absorption requires knowledge of the pressure, temperature, and concentration of $O_2$ and water vapor along the path of the signal; the total gaseous attenuation is calculated by integrating along this path. Much previous work (eg., Moore et al., 1982; Spencer, 1988) has shown that global *variations* in gaseous attenuation are small at Ku-band scatterometer frequencies. Moore et al. (1982) find that measured variations in $\sigma_0$ in clear-sky and light cloud conditions are due overwhelmingly to changes in ocean surface roughness. Furthermore, empirical model functions such as SASS-II, that are based on uncorrected spaceborne scatterometer data, already include the mean effects of gaseous attenuation. Correction of $\sigma_0$ measurements obtained in clear-sky or light cloud conditions is therefore not required, and the focus for this algorithm is in identifying and (where possible) correcting measurements obtained from heavy cloud and/or precipitating conditions. The correction desired is to clear-sky, rather than vacuum, conditions. Thus, for SWS, equation (3.3-3) can be approximated by

$$\sigma_{0CLEAR} = \sigma_{0MEAS} + 2\tau_{LIQ}(13.402) \quad (3.3-4a)$$

$$\tau_{LIQ}(13.402) = \sec\theta \int_0^H ((\alpha_{CLOUD}(13.402,z) + \alpha_{RAIN}(13.402,z))\,\mathrm{d}z \quad (3.3-4b).$$

Both scattering and absorption are responsible for the modification of Ku-band radiation by atmospheric liquid water. Expressions first derived by Mie can be used to calculate the extinction, scattering, and absorption efficiencies for water droplets or ice particles (see Ulaby et al., 1981). The Rayleigh approximation is accurate when the particle size (scaled by the index of refraction) is much smaller than the wavelength of the radiation. At 13.402 GHz (the SWS frequency), the Rayleigh approximation is valid for most cloud conditions and for light rain (1–2 mm/hr), while the full Mie scattering formulae must be used for most rain (Moore et al., 1982; Durden and Chapman, 1987). Given knowledge of atmospheric vertical profiles of temperature, liquid water density, and drop size distributions, the Mie and Rayleigh models (as appropriate) can be used to calculate $\tau_{LIQ}(13.402)$ and hence the atmospheric correction to $\sigma_{0MEAS}$. However, it is evident that neither the atmospheric profile information nor the integrated transmissivity can be inferred from single-frequency scatterometer backscatter measurements.

Brightness temperature ($T_B$ ) measurements of the ocean-atmosphere system acquired by multichannel microwave radiometers can be used to obtain information on a variety of atmospheric and sea-surface properties. The radiative transfer equation relating $T_B$ at the top of the atmosphere to environmental conditions for a non-scattering atmosphere in thermal equilibrium has been discussed extensively in the literature (e.g. Wentz, 1983; Stewart, 1985), and can be written

$$T_B(f,\theta,p) = (1-e(f,\theta,p))t^2(f,\theta)T_{ext} + (1-e(f,\theta,p))t(f,\theta)T_d(f,\theta) + T_u(f,\theta) + e(f,\theta,p)t(f,\theta)T_s \quad (3.3-5)$$

where $p$ is polarization, $\theta$ is the incidence or look angles (considered equal in the discussion below) relative to vertical, $t$ is the transmittance of the atmosphere, $e(f,\theta,p)$ is sea-surface emissivity (thus $(1-e)$ is reflectivity), and $T_s$ is sea-surface temperature. $T_{ext}$ is the brightness temperature of extraterrestrially generated downwelling radiation at the top of the atmosphere (for present purposes, $T_{ext} =\sim 3$ K due to the cosmic background radiation; galactic noise makes only a minor contribution and measurements contaminated by sun glint, which can dominate the entire signal with brightness temperatures exceeding 6000 K, are not used in the calculations). $T_u$ and $T_d$ are the brightness temperatures of the upwelling atmospherically generated radiation at the top of the atmosphere and the downwelling atmospherically

generated radiation at the sea surface:

$$T_u = \int_0^H T(z)\alpha(z)\exp[-\tau(z,H)\sec\theta]\sec\theta \mathrm{d}z \qquad (3.3-6a)$$

$$T_d = -\int_0^H T(z)\alpha(z)\exp[-\tau(0,z)\sec\theta]\sec\theta \mathrm{d}z, \qquad (3.3-6b)$$

$$\tau(z',z'') = \int_{z'}^{z''} \alpha(z)\mathrm{d}z \qquad (3.3-6c)$$

$$t = \exp[-\tau(0,H)]; \qquad (3.3-6d)$$

$T(z)$ is the temperature of the atmosphere at height $z$, $\tau$ is the optical depth, and $\alpha$ is the absorption coefficient. As discussed below, the emissivity and reflectivity of the sea surface is a function of wind speed; the brightnes temperature of the sea surface is therefore a function both of its thermodynamic temperature and the wind speed.

As noted by Wilheit et al. (1980) and Stewart (1985), although the mechanisms by which the atmosphere modifies (and emits) microwave radiation are well known, calculation of the absolute magnitudes of the absorption coefficients and brightness temperatures at frequencies of interest is dependent on knowledge of vertical profiles of quantities such as temperature, liquid water and water vapor densities, and drop size distributions. In addition, brightness temperatures (eqs. (3.3-5) and (3.3-6)) are dependent on surface environmental parameters such as sea-surface temperature and wind speed. Inversion of a finite set of brightness temperature measurements to yield environmental parameters is thus not unique.

In practice, however, useful environmental information can be obtained from $T_B$ data, and scatterometer radiometric corrections can be calculated, because studies based on forward calculations have shown that both $T_B$ and $\alpha$ are nearly insensitive to variations in vertical *profiles*; the basic sensitivities are rather to *vertically integrated* quantities. These analyses are described in detail in Wilheit and Chang (1980), Moore et al. (1982), Wentz (1983), Callahan (1990), and references therein. Atmospheric profiles were basedon idealized models and actual measurements from radiosondes at a variety of geographical locations and seasons. Furthermore, the strong frequency- and polarization-dependence of brightness temperature on physical phenomena (eg., Wilheit et al., 1980) approximately diagonalizes the full matrices and allows relatively simple inversions for (in some cases integrated) quantities of interest using only a small number of carefully chosen frequencies and polarizations.

Three basic approaches have been documented for utilizing the atmospheric profile/sea-surface environmental condition data and the forward calculation of the non-scattering radiative transfer equation for determining Ku-band atmospheric modification.

The approach used for the operational processsing of SASS data (Moore et al., 1982; Moore et al., 1983) utilizes brightness temperatures at single frequencies (18 or 37 GHz v-pol) and $T_s$ obtained from monthly-mean climatologies. A constant wind speed of 10 m/s is assumed for the purposes of calculating sea-surface emission. The forward calculations based on idealized atmospheric models and empirical relations between cloud liquid water/rain rates and Ku-band obsorption are used to establish a simple ($T_s$-dependent) polynomial regression between the excess brightness temperature at each radiometer frequency and Ku-band absorption. A decision algorithm is used to choose between Ku-band absorptions based on the 37 GHz brightness temperature (which is least affected by wind speed and $T_s$ errors, and is most sensitive to liquid water at low concentrations, but which saturate at relatively low atmospheric liquid water values) and those based on 18 GHz measurements (which are less sensitive, but saturate at much higher rain rates). If both the 37 and the 18 GHz calculated attenuations were large, the scatterometer measurements were flagged as being contaminated by excessive rainfall and neither corrected nor used in subsequent wind retrieval calculations.

The TOPEX/Poseidon approach (Callahan, 1990) similarly uses parameterizations relating measured $T_B$ to Ku-band absorption. A larger data base, composed of more than 6000 radiosonde atmospheric profiles from a variety of island stations was used for the forward calculations; calculations were performed for the 3 frequencies measured by the TOPEX/Poseidon TMR radiometer (18, 21, and 37 GHz) at its nadir viewing geometry. A statistical distribution of sea-surface temperatures centered on the surface air temperature from the radiosonde profile was used. For each profile, seven wind surface wind speeds (4, 8, 12, 16, 20, 24, and 28 m/s) were used to calculate surface emissivity based on a simple parameterization that TMR $T_B$ increased by 0.004 K for each m/s of near-surface wind speed above 7 m/s (simulations using other wind speed emissivity dependences conducted in support of the TOPEX/Poseidon development, suggested that the final results were relatively insensitive to details of the relation between wind speed and emissivity).

In contrast to the SEASAT scatterometer correction algorithm, which related $T_{Bex}$ at single frequencies to Ku-band attenuation, the TOPEX/Poseidon correction used empirically determined coefficients and linear

models relating measured ln(280-$T_B$ ) at each of the TMR frequencies to integrated water content, near-surface wind speed, and atmospheric path delay (highly sensitive to integrated water vapor and of primary interest for correction of the altimeter height measurement itself). Empirical coefficients were calculated for each of the wind speeds both for the entire profile data set and for five subsets based on overall path delay (water vapor). Nonlinearities neglected by the linear models were partially compensated by an iterative technique. Atmospheric transmissivity at Ku-band was modeled as a linear combination of path delay and integrated liquid water, again with coefficients calculated using the non-stratified full profile data set and forward calculations.

In the operational TOPEX processing, estimates of wind speed and integrated liquid water were calculated from coefficients determined using the full profile data base (no path delay stratification), followed by an initial estimate of path delay using wind-speed dependent coefficients based on regressions using the full data base. Refined estimates of path delay were then calculated from the measured $T_B$ , estimated path delay, and estimated wind speed by using appropriately averaged path-delay-stratified coefficients. The Ku-band transmissivity was then calculated as a linear combination of the final path delay estimate and the integrated liquid water estimate.

Wentz(1982) and Wentz et al. (1986) present a simple nonlinear model function relating selected radiometer $T_B$ to desired atmospheric integrated quantities, surface environmental properties, and atmospheric absorption. The methods by which the model function was determined based on SEASAT SASS, SEASAT SMMR, and radiative transfer theory is also presented in detail (thus allowing modification based on specific radiometer frequencies, such as for AMSR which operates at slightly different frequencies than the SMMR or SSM/I instruments, and for inclusion of a larger radiosonse data base for the forward calculations). Comparisons between $T_B$ data from the SMMR and simultaneous wind velocity measurements from the SASS instrument were used to establish the temperature-, wind speed-, and incidence angle-dependent form of the surface emissivity in the model. Accurate idealizations of the measured vertical profiles (eg., the use of a constant air temperature over a (frequency-dependent) effective height) was used in thed derivation to simplify the full radiative transfer equation. Wentz (1992) summarizes the model and presents a simple inversion technique for non-raining conditions using only 37 GHz (v-pol and h-pol) and 22 GHz (v- or h-pol)

$T_B$ measurements from the SSM/I (and climatological $T_s$ and air temperature data) to derive integrated atmospheric water vapor, 37 GHz liquid water attenuation, and wind speed. (As persented in Wentz (1992), the 37 GHz $T_B$ data are used to calculate wind speed and frequency-dependent opacity; the wind speed is then used, with the model function and 22 GHz $T_B$ , to calculate opacity at 22 GHz; finally the Rayleigh scattering law is used to relate 37 GHz and 22 GHz liquid water specific attenuations, and the two opacities are used to calculate 37 GHz liquid water attenuation and integrated water vapor). Using the Wentz et al. (1986) modifications to the earlier Wentz (1982) model, the integrated atmospheric liquid water content can be calculated; as there is an approximately linear relationship between liquid water absorption coefficients and frequency from 10–23 GHz (see Wentz et al. (1986) and Wentz (1982)), the liquid water attenuation at the SWS frequency of 13.402 GHz can thus be calculated in a straightforward manner.

Algorithmic Considerations: The atmospheric correction algorithm is the least mature of the SeaWinds science algorithms. Fundamental resolution incompatibilities between the SASS scatterometer and the SEASAT SMMR measurements precluded accurate correction of the SASS data. Atmospheric attenuation due to rain is negligible for the C-band ERS-1 scatterometer. The ADEOS-I mission will not have a multi-channel microwave radiometer on board, and thus it will not be possible to correct the NSCAT Ku-band $\sigma_0$ data for atmospheric effects (although it may be possible to flag specific spatial/temporal regions for likely rain contamination, based on analyses of co-orbiting (although not colocated) radiometer data from the DMWP SSM/I instruments). The SWS flight on ADEOS-II will thus represent the first opportunity to use colocated, high-resolution radiometer data to radiometrically correct Ku-band scatterometer measurements for atmospheric effects.

All of the methods described above are based, to some degree, on forward calculations using the radiative transfer equation for a non-scattering atmosphere in thermal equilibrium. They are thus not strictly valid for rain conditions, in which scattering from rain drops is expected to be significant. based on land data, Goldhirsh (1983) determined that rain rates exceeding 2 mm/hr occurred only 1% of the time, and rates exceeding 10 mm/hr ocurred only approximately 0.2% of the time. Although rain statistics over the ocean are presently not well known (additional information is expected following the flight of the TRMM mission), heavy rain rates over the ocean are expected to occur less frequently than over land. As noted above, rain

conditions are manifested as large liquid water attenuation values, expecially at 37 and 18 GHz. Based on research to be conducted in the coming months, specific attenuation values for rain flag assignment will be determined. Scatterometer $\sigma_0$ measurements contaminated by rain (based on the AMSR $T_B$ will be flagged, but will not be corrected.

Processing: Atmospheric correction/rain flagging is calculated for all open ocean (no land or ice) SWS wind vector cells for which sufficient AMSR data exist. The processing takes place as part of the wind retrieval processing from Level 2.0 (Global $\sigma_0$ Data) to Level 2.0 (Ocean Vector Winds).

(1) GROUPING/ICE FLAG: All AMSR $T_B$ measurements at relevant frequencies (at a maximum, 6.6–37GHz, both v- and h-pol are grouped according to their along-/cross-track coordinates (assigned in the same way as those for the $\sigma_0$ measurements, based on latitude and longitude locations). Depending on the specific atmospheric correction algorithm used, only a subset of the $T_B$ data (typically 18, 23, and 37 GHz) may be employed, along with a sea-surface temperature climatology. Use of radiometer $T_B$ data for measurement of sea ice concentration is well documented (cf. Gloersen et al., 1992) and typically involves use of $T_B$ ratios at 18 and 37 GHz (both h- and v-pol). Sea ice concentrations in excess of (TBD – typ. 5%) will cause $\sigma_0$ observations to be flagged as ice-contaminated and not processed further.

(2) SPATIAL AVERAGING: All $T_B$ data at each frequency/polarization within a wind vector cell is averaged linearly. More sophisticated area-weighted schemes and those involving extended-area interpolation to $\sigma_0$ locations will be investigated when details of the AMSR sampling pattern and Japanese $T_B$ processing approaches become known.

(3) ATTENUATION CALCULATION/RAIN FLAG: The averaged $T_B$ data are used with the chosen (TBD, but typically one of the three discussed above) to identify rain-contaminated cells or total atmospheric attenuation at 13.402 GHz. Attenuation values (dB) are added to $\sigma_0$ values prior to use of the $\sigma_0$ data for wind retrieval.

*3.4 Wind Retrieval*

Objective: The objective of the wind retrieval algorithm is to determine the wind velocity (speed and

direction) that is statistically consistent with both the set of nearly colocated $\sigma_0$ measurements and the model function relating $\sigma_0$, radar geometry, and vector winds.

Physical/Mathematical Basis: Although the wind retrieval algorithm plays a crucial role in scatterometer processing, it is a statistical, rather than physical, algorithm. If $\sigma_0$ measurements were perfect and perfectly colocated, if the model function were known precisely, and if $\sigma_0$ was a unique function of near-surface wind velocity and radar parameters, retrieval of wind velocity from three or more $\sigma_0$ measurements could be accomplished analytically. However, a statistical estimation scheme is required in the realistic case where $\sigma_0$ measurements are noisy and imperfectly colocated, the model function is neither perfectly known nor uniquely a relationship between $\sigma_0$ and winds, and even the radar parameters (eg. incidence and antenna pointing angles) are corrupted by errors.

From a statistical standpoint, wind retrieval represents the *"a posteriori"* problem, in which the true parameters of a statistical distribution must be estimated based on a finite set of observations. In the case of scatterometer wind retrieval, the difficulty lies fundamentally with the facts that the "observations" are noisy, the functional form of the statistical distribution from which they are drawn is not known exactly, and the observation set is composed of only a small number of measurements.

There is no unique "correct" method for solving the *a posteriori* estimation problem (cf. Jenkins and Watts, 1968). All methods require *a priori* specification of the sampling probability density function (pdf) for the observations, excepting some unknown values of the parameters. A set of observations is then substituted into the specified pdf yielding an analytic function (the "likelihood function") with the parameters of the original pdf as the variables. The appropriate local or global extrema of the likelihood function, corresponding to the most likely parameter values consistent with both the pdf and the measurements, are then identified. The "accuracy" of a given estimation scheme depends upon the accuracy with which the assumed pdf approximates the true pdf, and the robustness of the method to errors in the pdf specification.

Chi and Li (1988) conducted a detailed simulation study of seven *a posteriori* estimation schemes appropriate for the scatterometer problem, and concluded that a maximum likelihood estimation approach (Jenkins and Watts, 1968; Freilich and Pawka, 1987), first suggested in this context by Pierson (1984), was the best approach. The MLE wind retrieval algorithm was adopted for use with NSCAT, is presently being

utilized to process ERS-1 scatterometer data, and is the baseline for SWS processing. A brief derivation is presented below, based on Chi and Li (1988), Dunbar et al. (1988), and Long et al. (1994). An approximate pdf for the individual $\sigma_0$ measurements is first derived, and is related to the wind velocity through the model function. This is followed by specification of the joint pdf of a set of colocated measurements, which becomes the likelihood function for the estimator.

Each $\sigma_0$ "measurement" in the Level 2 product (see section 3.2) can be denoted by

$$z_i = \sigma_{0i}(\phi_i, \mathrm{p}_i, \theta_i) + \epsilon_i(\phi_i, \mathrm{p}_i, \theta_i), \qquad (3.4-1)$$

where $\sigma_{0i}$ is the value of $\sigma_0$ that would be measured by a perfect scatterometer instrument at the particular spatial location characterized by the radar look paramaters $(\phi_i, \theta_i)$ and polarization $\mathrm{p}_i$, and $\epsilon_i$ represents random errors. There are three types of errors that contribute to $\epsilon_i$ and that have been discussed extensievly in the literature:

(1) differential noise introduced by the instrument itself in the Doppler filter vs. noise filter chains;

(2) communication noise due to the (random) superposition of scatter from many scatterers located within the footprint; and

(3) radar noise, due to inaccurate knowledge of the quantities in the radar equation – this term includes inaccuracies in knowledge of $\phi_i$ and $\theta_i$ as well as calibration errors in the antenna gains, etc.

For the purposes of wind retrieval, it is assumed that $\epsilon_i$ is a gaussian random variable with zero mean and variance $V_{\epsilon_i}$ (ie., $\epsilon_i = N(0, V_{\epsilon_i})$). Long et al. (1988), Chi and Li (1988), and Long (1994) show that the variance for both digital Doppler fan-beam and pencil-beam instruments can be expressed as

$$V_{\epsilon_i} = \alpha\sigma_{0i}^2 + \beta\sigma_{0i} + \gamma, \qquad (3.4-2)$$

where the coefficients $\alpha,\ \beta,$ and $\gamma$ are functions of the instrument design and are slowly varying functions of $\phi$ and $\theta$. Importantly, $V_{\epsilon_i}$ depends on the *true* value of $\sigma_{0i}$, not on the measured values $z_i$ ; however, because of the slow variation of coefficients on azimuth and incidence angle, the measured values $\phi_i$ and $\theta_i$ can be used to evaluate $V_{\epsilon_i}$.

The true backscatter cross-section $\sigma_{0i}(\phi_i, \mathrm{p}_i, \theta_i)$ is related to the near-surface wind velocity by the model

function

$$\sigma_0(\phi, \mathrm{p}, \theta) = M(w, \chi; \theta, \mathrm{p}) \tag{3.4-3}$$

where the relative direction $\chi$ is related to the radar azimuth angle $\phi$ and the wind direction $\Phi$ through

$$\chi = \Phi - \phi. \tag{3.4-4}$$

Inaccurate knowledge of the model function results in a difference between the predicted $\sigma_0$ and the true cross-section corresponding to given values of the wind and radar parameters. The (unknown) model function inaccuracies are made explicit by defining

$$\sigma_{0\,Mi}(\phi_i, \mathrm{p}_i, \theta_i) = M(w, \chi_i; \theta_i, \mathrm{p}_i) + \epsilon_{Mi}, \tag{3.4-5}$$

where $\epsilon_{Mi}$ is also a zero-mean, normally distributed random variable with variance dependent on the true wind velocity and the radar parameters. As with the $\alpha,\ \beta,$ and $\gamma$ coefficients in (3.4-2), it is assumed that the *errors* in the model function vary sufficiently slowly with look geometry that an accurate estimate of the error variance can be obtained using the measured values $\theta_i$ and $\phi_i$ associated with the $\sigma_0$ cell.

For a given wind velocity $(w, \Phi)$, the residual $R_i$ for a measurement $z_i$ is defined

$$R_i(w, \Phi; \theta_i, \mathrm{p}_i) = z_i - \sigma_{0\,Mi}. \tag{3.4-6}$$

If it is assumed that the model function errors $\epsilon_{Mi}$ are independent of the $\sigma_0$ measurement errors $\epsilon_i$, $R_i$ is a normally distributed variable with zero mean and variance

$$V_{R_i} = V_{\epsilon_i} + V_{\epsilon_{Mi}}. \tag{3.4-7}$$

$V_{R_i}$ is clearly a function of the true value of $\sigma_{0i}$, rather than the measured value $z_i$ .

The conditional probability density function for $R_i$ associated with a single measurement $z_i$ (and given an assumed wind velocity) can thus be written

$$p(R_i|\sigma_0) = p(R_i|(w, \Phi)) = (V_{R_i})^{-1/2} \exp\left\{-(R_i)^2/2V_{R_i}\right\}. \tag{3.4-8}$$

Consider now the case of $N$ spatially and temporally colocated $\sigma_0$ measurements $z_i$ , $i = 1, \ldots, N$, all corresponding to a single, but unknown wind velocity $(w, \Phi)$. If it is assumed that each of the residuals is

independent, then the joint conditional probability is given by

$$p(R_1, \ldots, R_N|(w, \Phi)) = \prod_{i=1}^{N} p(R_i|(w, \Phi)). \qquad (3.4-9)$$

Maximum likelihood solutions correspond to the parameter values $(w, \Phi)$ which locally minimize $p$. The likelihood function is simplified with no loss of generality by taking the logarithm of (3.4-9) and discarding constants (only minima and their *relative* values are of interest), yielding

$$J_{MLE}(w, \Phi) = \sum_{k=1}^{N} \left\{ \left( \frac{z_k - M_k(w, \Phi)}{\Delta_k} \right)^2 + \ln \Delta_k \right\} \qquad (3.4-10)$$

where

$$\Delta_k = (V_{R_k})^{1/2} = \left( \alpha_k M_k^2 + \beta_k M_k + \gamma_k + V_{\epsilon_{Mk}} \right)^{1/2}. \qquad (3.4-11)$$

Local maxima of $J_{MLE}$ correspond to potential solutions; the relative likelihoods of 2 solutions are determined by the relative magnitudes of $J_{MLE}$.

Algorithmic Considerations: The shape of the model function and the nonlinearity of $J_{MLE}$ preclude *a priori* identification of the number and locations of minima. In principle, $J_{MLE}$ must be known for the full parameter space $(w, \Phi)$ before all local minima are identified. Evaluation of the objective function is computationally intensive, and thus algorithms should minimize the number of evaluations of $J_{MLE}$. In practice, the near-symmetry of the model function leads to continuous patterns of $J_{MLE}$ maxima as a function of direction, forming a "ridge" of large $J_{MLE}$ in wind velocity solution space. Extensive numerical simulations based on realistically noisy $\sigma_0$ measurements show that isolated local $J_{MLE}$ maxima (not along the "ridge") are found very infrequently. Although they are technically potential velocity solutions, the simulations demonstrate that in no cases do the non-ridge maxima correspond to the "correct" (ie., closest in direction to the true wind) solution, and they can therefore be discarded without overall loss of accuracy. An efficient ridge search routine has been developed for the NSCAT and ERS-1 processing (Dunbar et al., 1988). The Dunbar et al. routine is sufficiently general that it can be used with only a single minor change (related to initialization) for the SWS processing. Owing to the narrow range of incidence angles associated with SWS measurements, additional simplifications to the code will be examined for SWS.

Several key aspects of the MLE wind retrieval approach and algorithm require emphasis. The MLE approach is completely independent of the specific functional form adopted for the model function. As noted

in section 3.2, $\sigma_0$ "measurements" $z_i$ can be negative, especially when signal-to-noise ratios are small. All MLE equations derived above are in natural (not dB) units, and the gaussian distributions hypothesized for $z_i$ and $R_i$ allow both positive and negative values to be assumed. Negative $\sigma_0$ estimates can thus be accommodated in a fully consistent fashion.

The MLE retrieval algorithm is also functionally independent of the azimuthal distribution of the measurements $z_i$ . While the *accuracy* of the potential wind solutions is in part a function of the azimuthal diversity of the particular set of $z_i$ for a given wind cell, neither the MLE derivation nor the baseline NSCAT and SWS numerical algorithms rely on a particular azimuthal (or incidence angle) relationship among the $z_i$ .

There remains an inconsistency in the assumption that the $R_i$ for a given wind measurement cell are independent. In particular, model function errors may be correlated among several or all of the $R_i$ values. The effect is largest when the model function error is due to large-scale geophysical processes and/or when the azimuthal diversity between two $z_i$ measurements is not large (and there are azimuth-related model function errors). This problem was noted by Wentz (1991); resolution of the precise weighting function to use in the MLE objective function requires more detailed estimates of model function uncertainty than are available at present. Such improved uncertainty values are expected following the launch and validation of NSCAT.

Processing: Wind retrieval processing takes place for each 50 x 50 km cell in the alongtrack-crosstrack coordinate system.

(1) GROUPING: All open ocean $\sigma_0$ measurements whose centers fall within the along-cross track wind vector cell (wvc) are identified and collected, including all supplemental information in the Level 2.0 Global $\sigma_0$ product (eg., incidence angles, azimuths w.r.t. North, $K_p$ , etc.). Measurements of $\sigma_0$ that are flagged as land or ice are discarded, and are not included in wind retrieval processing. All AMSR brightness temperatures and associated data falling within the wvc are similarly grouped.

(2) ATMOSPHERIC CORRECTION: If more than TBD (3) open ocean $\sigma_0$ measurements having more than TBD (20° ) azimuth diversity (max - min) are in the wvc, available AMSR brightnes temperatures are

used to calculate atmospheric corrections (in dB) or identify uncorrectable rain conditions for the wvc as described in section 3.3. Further wind retrieval processing for this wvc does not take place if the uncorrectable rain flag is set. If no AMSR data are present, it is assumed that all $\sigma_0$ measurements are from clear sky conditions, and a "no-correction" flag is set.

(3) WIND SPEED INITIALIZATION: Starting with an assumed wind speed of 7.0 m/s and an assumed wind direction of 0° (w.r.t. N), determine wind speed at this direction yielding maximum $J_{MLE}$ (equation (3.4-10). Search is conducted with a wind speed resolution of TBD (0.5 m/s). Save maximum $J_{MLE}$ and associated wind speed.

(4) COARSE RIDGE SEARCH: Increment wind direction by TBD (10° ); using wind speed associated with maximum $J_{MLE}$ at previous direction, determine and save maximum $J_{MLE}$ at this direction by using simple three-point search strategy in wind speed with TBD (0.5 m/s) resolution. Search is clipped at 0 or 50 m/s (maximum extent of model function table). Continue to increment directions until all maximum speeds and objective function values are found at coarse directional resolution.

(5) DETERMINE RIDGE MAXIMA: Identify and rank local ridge maxima based on $J_{MLE}$ values from step (4). Keep up to 6 maxima.

(6) OPTIMIZE WIND SOLUTION: For each ridge maximum identified in (5), determine speed and direction associated with maximum $J_{MLE}$ value based on a local fine search with TBD (2° ) resolution. Use bi-quadratic interpolation to determine precise value of wind speed and direction corresponding to local maximum. (If interpolated solution falls outside data points used in the bi-quadratic interpolation, revert to velocity associated with fine search maximum.) Calculate $J_{MLE}$ value associated with interpolated (or reverted) velocity.

(7) EDIT AND RANK SOLUTIONS: Eliminate out-of-bounds wind speed maxima ($< 1$ m/s or $> 50$ m/s). Combine multiple solutions differing in speed and direction by less than TBD amounts. Rank remaining solutions by $J_{MLE}$ values. Save up to 4 solutions.

*3.5 Ambiguity Removal*

Objective: The objective of the ambiguity removal algorithm is to choose, from among the potential $(w, \Phi)$ solutions that (locally) maximized the objective function (see section 3.4), the unique vector that is closest in direction to the true wind velocity.

Physical Background: The wind retrieval processing described in section 3.4 produces a set of potential wind velocity solutions (known as "ambiguities"). The solution closest to the true wind velocity in the cell is denoted the "closest" or "correct" solution; however, as the solutions are vectors, rather than scalars, even the definition of "closest" is ambiguous – both the magnitude of the difference vector and the scalar direction difference are reasonable metrics. As noted by many authors (see Naderi et al., 1991 and references therein), ambiguities generally have nearly the same speeds, but vary widely in direction. For the purposes of this ambiguity removal discussion, the "closest" solution will be that whose direction is closest to the direction of the true wind velocity.

In addition to the ambiguities themselves, the wind retrieval algorithm produces associated values of the likelihood function $J_{MLE}$. Solutions with larger $J_{MLE}$ values can be interpreted as having greater apparent statistical consistency between the measurements and the associated solution vector than those with lower $J_{MLE}$. However, as noted in section 3.4, measurement errors (magnified by the small number of $\sigma_0$ measurements contributing to each wind vector cell), errors in specifying the expected statistical distributions of the $\sigma_0$ measurements, and model function inaccuracies all can contribute to inaccuracies in the relative $J_{MLE}$ values. Although the relative $J_{MLE}$ values at the extrema are *one* measure of the likelihood of a solution's validity, other methods of summarizing the likelihood function in the area of extrema are possible (Jenkins and Watts, 1968; Freilich and Pawka, 1987). Finally, the small upwind-downwind asymmetry of the model function leads in almost all cases to solutions separated in direction by approximately 180° , but having nearly identical values of $J_{MLE}$. Choice of a unique velocity solution at each wind vector cell thus cannot, in general, be made on the basis of $\sigma_0$ measurements falling only within that cell. Nonetheless, (as demonstrated in the case of the SASS data set in the early 1980's), unique vector winds are virtually required before they will be utilized by the general scientific community.

Several ambiguity removal techniques have been suggested since the flight of SASS, including subjective approaches (eg., Wurtele et al., 1982), assimilation of scatterometer data into atmospheric circulation models,

and fully objective techniques which rely on scatterometer data alone (see Schroeder et al., 1985 and Schultz, 1990 for reviews of previous published work). Importantly, all of the techniques explicitly or implicitly assume that wind velocity components are correlated over distances large compared with the resolution of a single wind measurement cell. While rapid changes occur along some axes (as in fronts), it is assumed that these features are roughly continuous when measured along other directions.

Extensive testing using simulated NSCAT and SWS data, as well as real ERS-1 C-band scaterometer data, has demonstrated that an approach based on use of a circular median filter (Dunbar et al., 1988; Schultz, 1990, Shaffer et al., 1991) is both effective and efficient. A modified median filter ambiguity removal algorithm will be used in the baseline processing of SWS data. Shaffer et al. (1991) present a detailed discussion of the median filter ambiguity removal technique adopted for NSCAT processing, and the SWS approach is similar in many respects. Therefore, only a brief summary of the basic derivation is presented here, with emphasis on the unique features of the SWS data and the changes to the NSCAT scheme that will be employed for SWS processing.

Median filters have long been used in image processing to identify and eliminate data corrupted by impulse noise while preserving edges and other features which have longer spatial correlation lengths. The concept of a median has been extended to circular data (such as directions) by several authors (cf. Mardia, 1972), and to vector data by Shaffer et al. (1991). The median $\mathbf{A}^*$ of a set of $N$ vectors $\mathbf{A}_i$ can be defined by

$$\mathbf{A}^* = \min_j \sum_{i=1}^{N} \|\mathbf{A}(j) - \mathbf{A}(i)\|, \quad 1 \le j \le N. \tag{3.5-1}$$

As noted by Shaffer et al., minimizing the sum of vector norms is robust to outlier values in a manner similar to the median of a set of scalars.

In the scatterometer processing, the output of the wind retrieval algorithm consists of a set of potential velocity solutions (each a vector) for each wind measurement cell within the swath. The full set of ambiguous solutions can thus be thought of as a two-dimensional field defined on a nearly rectangular (across-track, along-track) grid; at each grid point $(i, j)$, there are between 0 and 4 possible solutions, denoted $\{\mathbf{A}_{ij}^k\}$.

The median filter operates instantaneously on a rectangular subset of the full field, centered on location $(i, j)$ and having (odd) dimensions $N_x$ and $N_y$ in the across- and along-track dimensions. Given a two-

dimensional vector field $\mathbf{U}$ within the window, the weighted vector median is defined as

$$\mathbf{U}^* = \min_{m,n} \left[ \sum_{m=\max(i-h_x,1)}^{\min(i+h_x,N_x)} \sum_{n=\max(j-h_y,1)}^{\min(j+h_y,N_y)} W_{mn} \|\mathbf{U}_{mn} - \mathbf{U}_{xy}\| \right] \quad 1 \le m \le N_x, \quad 1 \le n \le N_y, \qquad (3.5-2)$$

where $W_{mn}$ is a general weight determining the contribution of each vector to the norm sum, and $h_q = (N_q - 1)/2$.

The objective is to select the ambiguity $\mathbf{A}_{ij}^p$ which is closest (in a norm sense) to the vector median $\mathbf{U}^*$, equivalent to determining $p$ such that

$$\mathbf{A}_{ij}^p = \min_{p} \left[ \sum_{m=\max(i-h_x,1)}^{\min(i+h_x,N_x)} \sum_{n=\max(j-h_y,1)}^{\min(j+h_y,N_y)} W_{mn} \|\mathbf{U}_{mn} - \mathbf{A}_{ij}^p\| \right] \quad 1 \le m \le N_x, \quad 1 \le n \le N_y. \qquad (3.5-3)$$

The filter is applied sequentially to each of the locations $(x, y)$ in the full field, with the outputs $\mathbf{U}^*$ used to construct a new solution field. After the filter has been passed over all locations in the full field, the original initial field is replaced by the median filtered field $\mathbf{U}^*$ and the process is repeated until it converges (no further changes) or a set number of iterations are completed.

It is clear from (3.5-3) that the fully ambiguous vector field must be initialized before the median filtering is performed, and that this initialization is critical to the ultimate success of the approach. As noted by several authors (eg. Schultz, 1990; Shaffer et al., 1991), most failures of the algorithm are associated with poor initializations. An obvious approach is to use as the initial field the top-ranked (most likely) ambiguity, and this is the initialization used in the baseline design for NSCAT. This approach has the advantage that it is fully autonomous, requiring no additional information beyond the scatterometer data. However, as noted in section 3.4, the upwind-downwind near-symmetry of the model function typically results in two ambiguities having similar (high) likelihood values but differing in direction by $\sim 180°$. Errors in the model function and the $\sigma_0$ measurements can result in reversing the relative likelihoods of these solutions, and if the errors are spatially correlated, large regions of the measurement swath can be incorrectly initialized with directions nearly 180° from the "correct" direction. As the median filter ambiguity removal algorithm is based on the implicit assumption that errors are isolated and that the tue field has relatively large correlation scales (along at least some axes), the median filter thus will return incorrect results if the initial field is systematically in error. Both Shaffer et al. (1991) and Schultz (1990) document and quantify this effect based on simulations,

and both note that autonomous initialization based on instrument skill requires a large ($\sim$ 60%), nearly uniform, instrument skill.

Such instrument skill levels are not present in the ERS-1 data set, and are not anticipated in the SWS data. The C-band model function at ERS-1 incidence angles has extremely small upwind-downwind asymmetry. The difficulty in the SWS case arises not, primarily, from the model function, but rather from the azimuthal distribution of the $\sigma_0$ measurements. As noted in previous sections (see figure 5), the azimuthal sampling for SWS varies systematically with cross-track distance. As shown in figure 7, this results in systematic variations in both the number of ambiguities associated with the solutions, and the instrument skill (the percentage of time that the highest-ranking ambiguity is the closest solution). Instrument skill alone, therefore, cannot be relied upon for initialization of the SWS data.

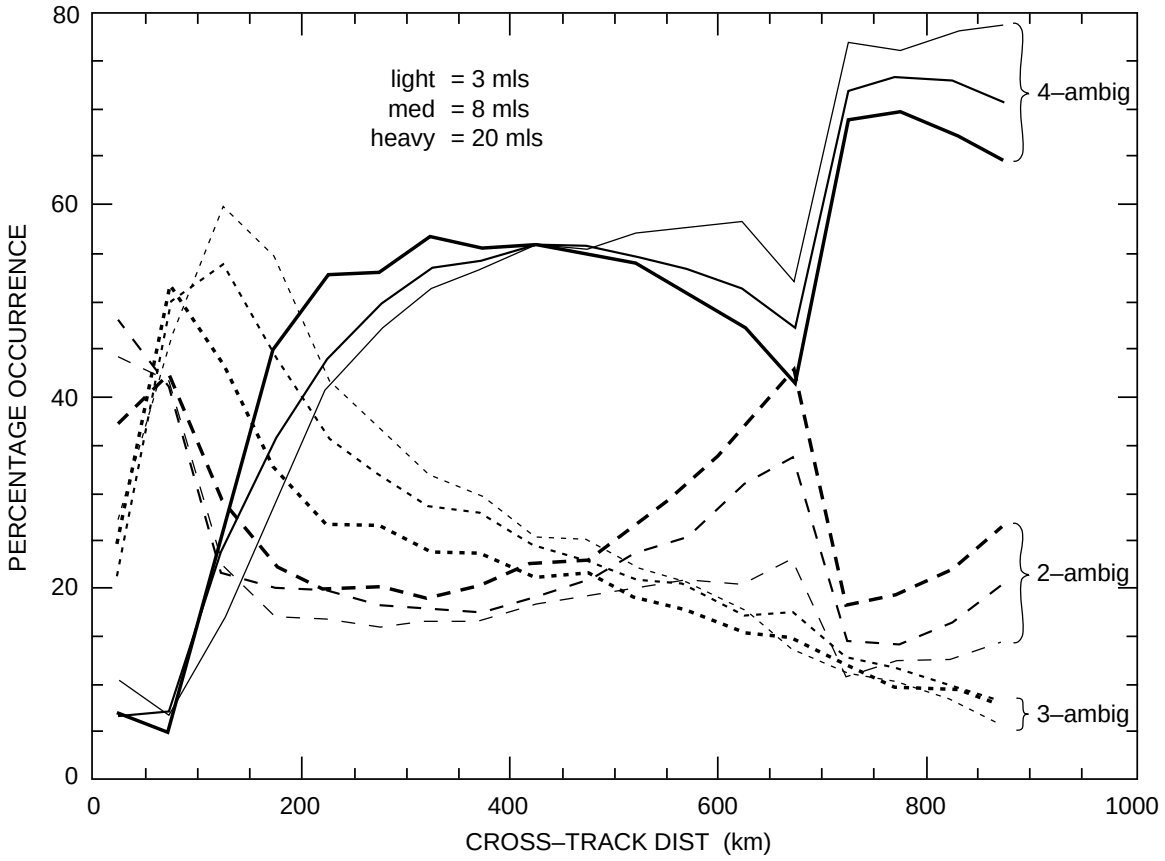


Figure 7. Relative variations in the number of ambiguities per solution as a function of cross-track distance for wind speeds of 3, 8, and 20 m/s.

Freilich and Dunbar (1994) have developed a limited initialization technique for ERS-1 and SWS ambiguity removal that makes use both of instrument skill and weak constraints provided by directional information derived from operational surface ("NWP") analyses. The NWP analyses are interpolated in space and time to the locations of the scatterometer wind solutions. The initial velocity solution at each location is chosen as the closest of the two top-ranked ambiguities to that direction (the minimization in this case is based on directions only, not vector norms). For large cross-track distances sampled by only the outer beam (typically containing 4 ambiguities at each point, each with equal likelihood), the solution closest in direction to the surface analysis is chosen.

Following this limited initialization, the median filter ambiguity removal algorithm is applied as described above. Importantly, *all* possible ambiguities are allowed in the median filter search at each point, not simply the top-ranked pair that were used for initialization. Much experience with the analysis of ERS-1 data and tests with simulated SWS measurements have demonstrated that the NWP-initialized median filter algorithm identifies the closest ambiguity in $> 97\%$ of all cases (excluding situations, discussed below, where significant fractions of the possible data in the measurement swaths are missing). The *limited* initialization, in which only the two top-ranked ambiguities are used, yields higher final skill than initializations in which the closest ambiguity to the surface analyses (independent of instrument skill) is used. This results from the fact that the operational surface analyses are smooth, and the set of all possible ambiguities typically spans the full directional space coarsely but nearly uniformally. Therefore, the median filter operating on the *fully* initialized field converges rapidly to a solution which resembles closely the surface analysis used for initialization. The *limited* initialization described above combines the NWP information with streamline directional information contained in the scatterometer solutions themselves, thus resulting in correct convergence of the median filter even in the presence of most NWP errors.

Exceptions and Future Development Work: As with all known ambiguity removal approaches that do not involve explicit assimilation of scatterometer data into dynamically constrained circulation models, the modified, initialized median filter algorithm is highly empirical. Several settable parameters (eg., the window dimensions $N_x$ and $N_y$, and the form of the weighting function $W_{mn}$) are available for tuning the algorithm based on the on-orbit performance of the SWS instrument. These parameters are set in the pre-launch

period based on simulations.

The median filter algorithm is known to be most prone to failure (ie., yielding low solution skill in large areas) when the operational analysis used for initialization is egregiously in error over large spatial errors, leading to large-scale systematic errors in the initialized wind field. However, experience has shown that the analysis errors must be $>\sim 90^\circ - 180^\circ$ over distances $> 1000 - 1500$ km in both the along-track and cross-track dimensions. While analysis errors of these *directional* magnitudes are often found, they do not typically extend over the large spatial areas necessary to cause failure of the ambiguity algorithm. Although the analyses have directional errors of smaller magnitudes that *do* extend over the required large areas, these do not substantially influence the (restricted) initialized field (and therefore the performance of the algorithm).

The algorithm can also fail when the filter window is missing substantial fractions of data. This effect occurs most often near the edges of the swath and near coasts. The skill of the algorithm in the presence of substantial missing data is difficult to quantify, as it depends on the overall percentage of missing data, the distribution of the data that *do* exist within the window, the true synoptic conditions, and the accuracy of the initialized field. Although a complete set of simulation studies will not be carried out to quantify the problem, a more limited set of simulations will be conducted to bound the effect; this may result in modifications such as caution flags for cases where the total number of data in a filter window fall below a set threshold.

Processing: Ambiguity removal processing is applied to an entire SWS rev (South pole to South pole).

(1) LOAD DATA: All wind vector cell data output from wind retrieval processing (including velocities for all ambiguities, likelihoods) for the entire rev are placed in a two-dimensional along-/cross-track coordinate system based on coordinates assigned previously. Two additional major along-/cross-track arrays ("Initial" and "Output" are created with the same dimensions.

(2) INITIALIZE: Operational surface wind analyses are interpolated to the locations of each wind vector cell (wvc) for which SWS data exist. The Initial wind field is composed of the indicator to the first- or second-ranked ambiguity, whichever is closest to the wind direction of the interpolated operational analysis.

For cases where all ambiguities have equal likelihoods, the initial vector is that ambiguity closest to the interpolated operational analysis direction.

(3) MEDIAN FILTER: A median filter with specified along-, cross-track dimensions (TBD – typ. 7 x 7) is centered on each array location for which SWS vector wind solutions exist. If a sufficient number of SWS vector wind solutions is present within the filter, the ambiguity identifier satisfying the median equation (3.5-3) is copied into the Output array. This process continues for all SWS wind solutions in the along-/cross-track rev array.

(4) COMPARISON: If the contents of the "Initial" and "Output" arrays (composed of selected ambiguity indicators) are not identical, the Output array is copied into the Initial array.

(5) ITERATION: Steps (3) and (4) are repeated until the Output and Input arrays are identical (convergence) or until a TBD (typ. 30) number of iterations have occurred.

(6) OUTPUT: The selected ambiguity in the Level 2.0 product is flagged. Separate flags are set for Level 2.0 wind vector cells for which no selection was made (insufficient number of solutions within median filter window, or non-convergence).

## 4. Validation

The indirect nature of scatterometer wind measurements necessitates careful pre- and post-launch instrument and geophysical calibration/validation. Of particular importance in the context of this ATBD are the post-launch $\sigma_0$ calibration and beam-balancing, model function refinement, and quantification of the wind speed and direction accuracies for both the closest and chosen ambiguities (corresponding to validations of the basic wind retrieval and ambiguity processing, respectively). Proposed approaches for each of these steps are outlined below. Each major algorithm validation will be based on multiple analyses using independently measured auxiliary or in-situ data (e.g., from open-ocean meteorological buoys or ground receiving stations), direct comparisons with contemporary, colocated measurements acquired by other spaceborne instruments (e.g., the NSCAT and ERS scatterometers or the AMSR radiometer), and quantitative comparisons with operational or research models (making use of the global ocean coverage of the model predictions while minimizing the impacts of, and sensitivities to, errors in the model formulations and fields).

### *4.1 $\sigma_0$ Validation and Beam Balancing*

Post-launch, end-to-end validation of the $\sigma_0$ processing (section 3.2) will be accomplished using ground receiving stations, analysis of backscatter measurements from extensive homogeneous, isotropic targets (such as the Amazon forest), and analysis of global open-ocean measurements utilizing approximate knowledge of the Ku-band model function and statistics of the imaged wind velocity distribution based on operational numerical weather prediction surface analyses.

The primary objective of the $\sigma_0$ validation is the identification and correction of time-independent relative $\sigma_0$ errors between the two SeaWinds beam, as well as any systematic azimuthally dependent errors (resulting, for instance, from unanticipated field of view obstructions in the spacecraft's actual on-orbit configuration). Although correction of absolute $\sigma_0$ biases is desirable, such errors can be easily corrected through refinement of the empirical model function tables used in the SWS wind retrieval processing, as discussed in section 4.2 below.

The $\sigma_0$ validation analysis will be based on data acquired over spatially extensive regions having homogeneous, isotropic scattering characteristics such as the Amazon jungle. Details on the analysis techniques

and examples of reults from the Seasat and ERS-1 spaceborne fan-beam scatterometers are described in Long and Skouson (1996) and references therein. The pencil-beam SeaWinds instrument differs from previous fan-beam instruments in that each antenna images at a single incidence angle, and it is thus not possible to perform beam balancing by directly comparing mean backscatter values acquired by different antennas at the same incidence angles. However, detailed analyses of the extent and azimuthal scattering properties of the Amazon Forest will be conducted early in the NSCAT mission as part of the NSCAT post-launch calibration and validation activities, and similar analyses will be undertaken using NSCAT data near the launch of SeaWinds. Significant ($> 0.2dB$) deviations between Amazon Forest backscatter cross-sections and azimuthal dependences measured by SeaWinds (as compared with NSCAT measurements at similar incidence angles) will indicate calibration errors in the SeaWinds $\sigma_0$ measurements.

Highly sensitive and well-calibrated ground receiving stations were used to help calibrate the ERS-1/2 scatterometers (LeComte and Attema, 1993) and will be employed in the NSCAT calibration campaigns. These stations directly measure the power that reaches the Earth's surface as the instrument passes over the station's site. By comparing the received power (after correction for clear-air atmospheric absorption effects) with the on-baord measurement of transmitted power, the effective antenna gain pattern can be determined given a sufficient number of satellite overpasses.

Recently, Freilich et al. (1996) presented a quantitative technique for performing relative antenna calibration for fan-beam scatterometers using low-order statistics of open-ocean measured $\sigma_0$ and approximate auxiliary information on the model function and the distributions of wind speed and relative azimuth derived from operational numerical weather prediction surface analyses. The approach is highly cost-efficient (requiring no additional scatterometer data acquisition beyond the ocean measurements used for wind retrieval) and utilizes $\sigma_0$ data having precisely the dynamic range of the ocean signals. In addition, Freilich et al. (1996) demonstrated that the method was relatively insensitive to realistic model function and operational surface analysis errors. When tested using C-band data from the C-band ERS-1 scatterometer, the approach yielded relative beam balancing error estimates good to $< 0.2$ dB from as little as 3 weeks of data. Although modifications to the Freilich et al. (1996) beam balancing analysis are required to accommodate the pencil-beam measurement geometry of SeaWinds, the approach will benefit from the accurate knowledge

of the Ku-band model function acquired during the NSCAT mission.

### *4.2 "Ambiguous" Vector Wind Estimates and Model Function*

Although the measurement requirements for SeaWinds apply to the unique wind velocity determined by the wind retrieval (see section 3.4) and ambiguity removal (see section 3.5) processing algorithms, it is possible to validate the wind retrieval and ambiguity removal algorithms separately. This subsection addresses validation of the wind retrieval processing leading to multiple vector wind solutions, while subsection 4.3 below addresses the ambiguity removal processing.

The primary validation of the SeaWinds wind retrieval algorithms will be based on comparisons between ambiguous SWS wind velocities and spatially and temporally colocated in situ wind measurements from operational, open-ocean meteorological buoys. Similar investigations have been conducted for the Seasat (Freilich, 1986; Woiceshyn et al., 1986) and ERS-1 scatterometers (Halpern et al., 1993; Bentamy et al., 1994; Graber et al., 1996). An extensive buoy network exists off North America; the Japanese Meteorological Agency maintains a similar network around Japan. In addition, the TOGA/TAO buoy array in the equatorial Pacific provides measurements in the climatically important tropics, and it is expected that a similar network will be established in the low-latitude Indian Ocean by the end of this decade. (See Graber et al., 1996 for a compilation of existing buoys and details on buoy measurement accuracies.)

Many previous scatterometer-buoy validations have directly used the buoy wind speeds and directions, without correction for the altitude of the anemometer and the effects of local stratification (recall that the scatterometer measurements correspond to neutral stability wind velocities at fixed (typically 10 or 19.5 m altitude). For SWS, wind velocities measured by the buoy anemometers will first be corrected to neutral stability winds at a standard 10 m altitude as specified in Liu and Blanc (1984), using buoy measurements of auxiliary environmental variables (sea-surface and air temperatures, humidity, etc.; cf. Freilich, 1986, and Graber et al., 1996).

The spatial and temporal variability of wind field requires that the satellite and buoy wind measurements be colocated in both space and time. Freilich (1986) and Monaldo (1988) and references therein discuss expected wind speed differences resulting solely from the incompatibility of the buoy (temporal averages at

a fixed location) and scatterometer (instantaneous spatial averages) measurements. Pierson (1983; see also Freilich, 1986) discusses the buoy temporal averaging required to minimize differences due to the measurement incompatibilities. It is expected that colocations will be restricted to maximum temporal differences of 60 min. and spatial differences of 100 km.

The wind velocity of ambiguity closest to the measured buoy correction will be used in the comparisons. The SWS science requirements (Table 1) require both speed and directional accuracies to be quantified, and the model function is likewise defined in terms of wind speed and (relative) direction. Separate buoy comparisons of speed and direction will therefore be examined. Recently, however, Freilich (1996) investigated the effects of random component errors on vector magnitude comparisons and concluded that the random errors will cause apparently systematic wind speed errors if standard least squares comparison analyses are performed. Freilich (1996) proposed a more sophisticated nonlinear comparison analysis technique that allows simultaneous solution for systematic as well as random errors; the approach was tested using both Seasat and ERS-1 scatterometer-buoy comparisons. The method will be further refined during the NSCAT post-launch validation campaign.

In addition to comparisons with high quality buoy measurements, the SWS wind velocities will be compared with spatially and temporally colocated velocity and speed estimates from co-orbiting instruments, such as the earlier-generation NSCAT and ERS-1/2 scatterometers, the operational SSM/I microwave radiometers, and wind speeds calculated from the AMSR on ADEOS-II. While the colocation and comparison analyses are basically similar to those described above for the scatterometer-buoy comparisons, none of the satellite instruments can be considered the "standard" (in contrast with the buoy measurements). In particular, explicit account must be taken of errors in both the SWS and comparison measurements.

While the primary product of the "ambiguous" wind retrieval validation is the quantification of errors (bias, gain, and random) in the SWS wind velocities, acquisition and analysis of sufficient data spanning a large range of the parameter space (wind speed, relative wind direction, and incidence angle) will allow the model function to be refined and will result in improved wind retrieval accuracy. Bentamy et al. (1994) have used buoy data to develop a C-band model function for the ERS-1 scatterometer. Freilich and Dunbar (1993*a,b*) have developed a fully empirical approach for deriving model functions based on global comparisons

with large quantities of surface wind analyses from operational numerical weather prediction products. Straightforward extensions to the Freilich and Dunbar methodology also allow the influences of subsidiary geophysical processes (e.g., sea-surface temperature, long wave conditions, etc.) to be quantified. Both approaches will be used in the NSCAT geophysical validation campaigns and will be applied to SWS data in the (unlikely) event that the NSCAT Ku-band model function is found to be inadequate for SWS.

### *4.3 Ambiguity Removal*

Quantitative validation of the ambiguity removal algorithm is the most difficult validation task associated with scatterometry. Direct validation requires a colocated, independent measurement of wind direction. Such correlative data can at this time only be acquired by meteorological buoys. Buoy comparisons for the purpose of quantifying ambiguity removal skill are essentially the same as those described in section 4.2 above, with the exception that the buoy measurements are compared with the "selected," rather than the closest, scatterometer ambiguity, and the relevant statistic is the percentage of measurements in which the selected ambiguity is, in fact, the ambiguity closest in direction to the buoy wind direction.

Long (1993) developed an alternate wind retrieval/ambiguity approach based on direct assimilation of $\sigma_0$ measurements into a simple near-geostrophic surface wind model. Of relevance to the present discussion, the Long (1993) method can be modified to serve as a quality check on the classical, point-wise ambiguity removal methods of section 3.5. While tests with the Seasat and ERS-1 data sets have indicated that the method is not perfect, it has shown great promise for identifying both isolated and spatially coherent ambiguity removal errors. The approach will be further refined during the NSCAT validation campaign and will be applied to the SWS data if its performance can be well quantified.

## REFERENCES


Bentamy, A., Y. Quilfen, P. Queffeulou, and A. Cavanie, Calibration of the ERS-1 scatterometer C-band model. *IFREMER Tech. Rep. DRO/OS-94-01*, 72pp., 1994.

Boggs, D.H., SEASAT Geophysical Data Record (GDR) Users Handbook – Scatterometer, JPL D-129, 1982.

Chi, C.-Y. and F.K. Li, A comparative study of several wind estimation algorithms for spaceborne scatterometers, *IEEE Trans. Geosci. and Rem. Sens.*, **26**, 115–121, 1988.

Donelan, M.A. and W. J. Pierson, Radar scattering and equilibrium ranges in wind-generated waves with application to scatterometry, *J. Geophys. Res.*, **92**, 4971–5029, 1987.

Dunbar, R.S., S.V. Hsaio, and B.H. Lambrigtsen, Science algorithm specifications for the NASA Scatterometer Project, *JPL D-5610* (2 vols.), 1988.

Durden, S.L. and B. Chapman, Excessive Attenuation Flagging for NSCAT, JPL IOM 3343-87-354, 1987.

Elachi, C., *Spaceborne Radar Remote Sensing: Applications and Techniques*, Inst. Elect. and Electron. Eng., 255 pp., 1988.

Freilich, M. H., Satellite scatterometer comparisons with surface measurements: Techniques and Seasat results, *Proc. Workshop on ERS-1 Wind and Wave Calibration*, ESA SP-262, 57–62, 1986.

Freilich, M.H., Validation of vector magnitude data sets: Effects of random component errors. *J. Atmos. Ocean. Tech.* (submitted 3/96), 1996.

Freilich, M.H., H. Qi, and R.S. Dunbar, Scatterometer beam balancing using open-ocean backscatter measurements. *J. Atmos. Ocean. Tech.* (submitted 7/96), 1996.

Freilich, M. H., and R. S. Dunbar, Derivation of satellite wind model functions using operational surface wind analyses: An altimeter example, *J. Geophys. Res.*, **98**, 14,633–14,649, 1993*a*.

Freilich, M.H. and R.S. Dunbar, A preliminary C-band scatterometer model function for the ERS-1 AMI instrument. *Proc. First ERS-1 Symposium – Space at the Service of Our Environment*, Cannes, France, *ESA SP-359*, 79–84, 1993*b*.

Freilich, M.H. and S.S. Pawka, Statistics of $S_{xy}$ estimates, *J. Phys. Oceanogr.*, **16**, 741–757, 1987.

Gilhousen, D.B., A field evaluation of NDBC moored buoy winds, *J. Atmos. Ocean. Tech.*, **4**, 94–104, 1987.

Gloersen, P., W.J. Campbell, D.J. Cavalieri, J.C. Comiso, C.L. Parkinson, and H.J. Zwally, *Arctic and Antarctic Sea Ice, 1978–1987: Satellite Passive-microwave Observations and Analysis*, NASA SP-511, 290pp., 1992.

Goldhirsh, J., Rain cell size statistics as a function of rain rate for attenuation modelling. *IEEE Trans. Ant. Propag.*, **AP-31**, 799–801, 1983.

Graber, H. C., N. Ebuchi, and R. Vakkayil, 1996: Evaluation of ERS-1 scatterometer winds with wind and wave ocean buoy observations. *RSMAS Tech. Rep.,* RSMAS 96-xxx, University of Miamai, Fl., xx pp.

Halpern, D., M.H. Freilich, and R.S. Dunbar, Evaluation of two January-June 1992 ERS-1 AMI wind vector data sets. *Proc. First ERS-1 Symposium – Space at the Service of Our Environment*, Cannes, France, *ESA SP-359*, 135–140, 1993.

Jenkins, G.M. and D.G. Watts,*Spectral Analysis and Its Applications*, San Francisco, Holden-Day, 525 pp., 1968.

Jet Propulsion Laboratory, NASA Scatterometer Mission Requirements, JPL-D2676, Rev. A, 14pp.

Jet Propulsion Laboratory, Science and Mission Requirements and Standard Data Products, JPL-D10965, 9pp.

Kirimoto, T. and R.K. Moore, Scanning wind-vector scatterometers with two pencil beams, in *Proc. Conf. on Remote Sensing of Oceans and Atmospheres*, NASA Conf. Pub. 2303, 89–97, 1985.

LeComte, P. and E.P.W. Attema, Calibration and validation of the ERS-1 wind scatterometer. *Proc. First ERS-1 Symposium – Space at the Service of Our Environment*, Cannes, France, *ESA SP-359*, 19–29, 1993.

Liu, W. T., and T. V. Blanc, The Liu, Katsaros, and Businger (1979) bulk atmospheric flux computational iteration program in FORTRAN and BASIC, *NRL Memo. Rept. 5291*, 16pp., 1984.

Long, D.G., Wind field model-based estimation of Seasat scatterometer winds. *J. Geophys. Res.*, **98,** 14,651–14,668, 1993.

Long, D.G., $K_p$ for pencil beam scatterometers, *MERS Tech Rep. MERS 92-004*, Brigham Young University, 19 pp., 1994.

Long, D.G., C.-Y. Chi, and F.K. Li, The design of an onboard digital Doppler processor for a spaceborne scatterometer, *IEEE Trans. Geosci. Rem. Sens.*, **26**, 869–878, 1988.

Long, D.G. and G.B. Skouson, Calibration of spaceborne scatterometer using tropical rain forests. *IEEE Trans. Geosci. Rem. Sens., 34*, 413–424, 1996.

Mardia, K.V., *Statistics of Directional Data*, New York: Academic Press, 357 pp., 1972.

Monaldo, F., Expected differences between buoy and radar altimeter estimates of wind speed and significant wave height and their implications on buoy-altimeter comparisons. *J. Geophys. Res.*, **93,** 2285–2302, 1988.

Moore, R.K., I,J, Birrer, E.M. Bracalante, G.J. Dome, and F.J. Wentz, Evaluation of atmospheric attenuation from SMMR brightness temperature for the SEASAT satellite scatterometer, *J. Geophys. Res.*, **87**, 3337–3354.

Moore, R.K., A.H. Chaudry, and I.J. Birrer, Errors in scatterometer-radiometer wind measurement due to rain, *IEEE J. Ocean. Eng.*, **OE-8**, 37–49, 1983.

Naderi, F.M., M. H. Freilich, and D.G. Long, Spaceborne radar measurement of wind velocity over the ocean – an overview of the NSCAT scatterometer system, *Proc. IEEE*, **79**, 850–866, 1991.

Pierson, W. J., 1983: The measurement of the synoptic scale wind over the ocean. *J. Geophys. Res.*, **88,** 1683–1708.

Pierson, W.J., A Monte-Carlo comparison of the recovery of winds near upwind and downwind from the SASS-I model function by means of the sum of squares algorithm and a maximum likelihood estimator, *NASA Cont. Rep. 3839*, 1984.

Pierson, W.J., Examples of, reasons for, and consequences of the poor quality of wind data from ships for the marine boundary layer: implications for remote sensing, *J. Geophys. Res.*, **95**, 13,313–13,340, 1990.

Schroeder, L.C., W.L. Grantham, E.M. Bracalante, C.L. Britt, K.S. Shanmugam, F.J. Wentz, D.P. Wylie, and B.B. Hinton, Temoval of ambiguous wind directions for a Ku-band wind scatterometer using three different azimuth angles, *IEEE Trans. Geosci. Rem. Sens.*, **23**, 91–99, 1985.

Schultz, H., A circular median filter approach for resolving directional ambiguities in wind fields retrieved from spaceborne scatterometer data, *J. Geophys. Res.*, **95**, 5291–5303, 1990.

Shaffer, S.J., R. S. Dunbar, S.V. Hsaio, and D.G. Long, A median-filter-based ambiguity removal algorithm for NSCAT, *IEEE Trans. Geosci. Rem. Sens.*, **29**, 167–173, 1991.

Spencer, M.W., Seawinds SES Filtering Requirements, *JPL IOM-3347-94-002*, 14 Jan 1994.

Stewart, R.H., *Methods of Satellite Oceanography*, Univ. of Cal. Press, Berkeley, CA., 360 pp., 1985.

Ulaby, F.T., R.K. Moore, and A.K. Fung, *Microwave Remote Sensing: Active and Passive – Vol. 1*, 456 pp., 1981.

Ulaby, F.T., R.K. Moore, and A.K. Fung, *Microwave Remote Sensing: Active and Passive – Vol. 2*, 457–1064, 1982.

Ulaby, F.T., R.K. Moore, and A.K. Fung, *Microwave Remote Sensing: Active and Passive – Vol. 3*, 1065–2162, 1986.

Wentz, F.J., A simplified wind vector algorithm for satellite scatterometers, *J. Atmos. Oceanic Technol.*, **8**, 697–704, 1991.

Wentz, F.J., A model function for ocean microwave brightness temperatures, *J. Geophys. Res.*, **88**, 1892–1908, 1983.

Wentz, F.J., Measurement of oceanic wind vector using satellite microwave radiometers, *IEEE Trans. Geosci. and Rem. Sens.*, **30**, 960–972, 1992.

Wentz, F.J., S. Peteherych, and L.A. Thomas, A model function for ocean radar cross-sections at 14.6 GHz, *J. Geophys. Res.*, **89**, 3689–3704, 1984.

Wentz, F.J., L.A. Mattox, and S. Peteherych, New algorithms for microwave measurements of ocean winds: Applications to SEASAT and the Special Sensor Microwave Imager, *J. Geophys. Res.*, **91**, 2289–2307, 1986.

Wilheit, T.T., A.T.C. Chang, and A.S. Milman, Atmospheric corrections to pssive microwave observations of the ocean, *Bound. Layer Met.*, **18**, 65–77, 1980.

Wilheit, T.T. and A.T.C. Chang, An algorithm for retrieval of ocean surface and atmospheric parameters from the observations of the scanning multichannel microwave radiometer, *Radio Science*, **15**, 525–544, 1980.

Woiceshyn, P. M., M. G. Wurtele, D. H. Boggs, L. F. McGoldrick, and S. Peteherych, 1986: The necessity for a new parameterization of an empirical model for wind/ocean scatterometry. *J. Geophys. Res.*, **91,** 2273–2288.

Wurtele, M.G., P.M. Woiceshyn, S. Peteherych, M. Borowsky, and W.S. Appleby, Wind direction alias removal studies of Seasat scatterometer-derived wind fields, *J. Geophys. Res.*, **87**, 3365–3377, 1982.

Young, J,D, and R.K. Moore, Active microwave measurement from space of sea-surface winds, *IEEE J. Ocean. Eng.*, **OE-2**, 309–317, 1977.